STARS

Electronic Theses and Dissertations, 2004-2019

2009

Structural Analysis And Active Vibration Control Of Tetraform Space Frame For Use In Micro-scale Machining

Kevin Knipe
University of Central Florida

Part of the Mechanical Engineering Commons

Find similar works at: https://stars.library.ucf.edu/etd

University of Central Florida Libraries http://library.ucf.edu

STARS Citation

STRUCTURAL ANALYSIS AND ACTIVE VIBRATION CONTROL OF
TETRAFORM SPACE FRAME FOR USE IN MICRO-SCALE MACHINING

by

KEVIN KNIPE
B.S. The Ohio State University, 2007

A thesis submitted in partial fulfillment of the requirements
for the degree of Master of Science
in the department of Mechanical, Materials, and Aerospace Engineering
in the College of Engineering and Computer Science
at the University of Central Florida
Orlando, Florida

Fall Term
2009

ABSTRACT

This research thesis aims to achieve the structural analysis and active vibration damping of the Tetraform machining structure. The Tetraform is a space frame made up of four equilateral triangles with spherical masses at the four vertices. This frame was originally developed for grinding of optical lenses and is now being adapted for use in micro-precision milling. The Tetraform is beneficial to the milling process due to its exceptionally high dynamic stiffness characteristics, which increases the machining stability and allows for higher material removal rates and accuracy. However, there are still some modes of vibration that are critical to the milling process and need to be dampened out.

Under operating conditions of many structures, resonant modes of vibration can easily be excited which often lead to structural failure or significant reduction in operating performance. For the milling application, resonant frequencies of the machining structure can severely limit the milling process. The goal of the presented research is to increase surface and subsurface integrity with optimal material removal rate and least possible machining vibration, while maintaining accurate precision and surface finish. The vibrations from the machine tool not only affect the quality of the machined part but also the machine tool itself, since the cutting tool is susceptible to break or wear quickly when operating at high vibration modes, thus inevitably decreasing tool life.

Vibration control has gained considerable attention in many areas including aerospace, automotive, structural, and manufacturing. Positive Position Feedback (PPF) is a vibration

control scheme that is commonly used for its robust stability properties. A PPF controller works as a low pass filter, eliminating instability from unmodeled higher-frequency modes. The PPF controller concept is used in developing an active vibration control scheme to target the critical frequencies of the Tetraform. The controller is implemented with use of piezoelectric actuators and sensors, where the sensors are bonded to the opposing sides of the beams as the actuators, allowing for the assumption of collocation. The sensor/actuator pairs are placed at an optimal location on the Tetraform with high modal displacements for all the critical frequencies.

Multiple finite element models are developed in order to analyze the structural dynamics and allow for controller design. A model is developed in the finite element software ANSYS and is used to obtain the Tetraform's dynamic characteristics, which include natural frequencies and mode shapes. This model is also used to visualize the changes in mode shapes due to structural modifications or different material selections. Other models are also developed in Matlab and Simulink. This consists of the creation of a finite element model which is then converted to state space. The piezoelectric transducers are included in this model for the input and output of the state space model. This model can be used for controller design where the goal is to create maximum decibel reduction at critical frequencies while attempting to minimize controller effort.

ACKNOWLEDGMENTS

First, I would like to express my greatest appreciation to my advisor, Dr. Chengying Xu. I am very thankful for the amazing opportunity she had granted me with being able to work with her on this exciting project. I am also thankful for the time, effort, and guidance that she has invested into me and my research studies.

Next, I would like to thank Dr. David Nicholson for his guidance with the finite element model development of the Tetraform and Mr. Alex Pettit for his assistance with obtaining the experimental frequency responses through the impact hammer method. Their help was essential to the development of this project.

Also, I would like to thank my committee members, as a whole, for taking time out of their very busy schedules to help me through the thesis process. Additionally, I would like to thank my fellow lab members for always being there to help.

Finally, but certainly not least, I would like to thank my parents. They have always been there to support me in any way throughout my college career. Without them, none of my education would have been possible.

TABLE OF CONTENTS

LIST OF FIGURES

LIST OF TABLES

1 CHAPTER 1 – INTRODUCTION

There are two main goals of this research. They are to analyze the Tetraform space frame and to develop a method of vibration control of the Tetraform intended to optimize the machining process. The Tetraform is a tetrahedral frame used to hold a high speed spindle for micro-scale milling. It is essential to the machining process to have minimal vibrations in the structure holding the spindle. The Tetraform prototypes were analyzed to determine how susceptible the structure is to vibration. An active vibration control scheme was then designed to dampen out natural frequencies that are critical to the machining process.

Structural vibration is very critical to machining performance. When machining on the micro/nano scale, it is desirable to operate at a high material removal rate to increase economic efficiency. The goal of present research is to increase surface and subsurface integrity with satisfactory material removal rate by decreasing the vibrations of the tool holding structure. This helps to prevent fatigue cracking and increase part life. Structural vibrations play an important role in the ability to machine at a very high material removal rate while maintaining high precision and surface finish. The vibrations felt by the machine tool not only affect the quality of the machined part but also the machine tool itself, since the cutting tool is susceptible to pitting and wear when operating at high speeds, thus inevitably decreasing tool life.

While the Tetraform displays favorable dynamic stiffness compared to the more commonly used machining structures [4][5], there is still a need to dampen out certain modes of

vibration. For this, an active vibration control scheme was developed to target such frequencies. The Tetraform is converted to a smart-structure by implementing piezoelectric sensors/actuators. The positions of the sensors/actuators are chosen to effectively dampen out the modes of vibration that are most critical to the machining process, i.e., induces the largest displacement to the spindle holder. The actuators and sensors will be collocated to best obtain a displacement signal for the controller. Positive Position Feedback is then used to control the input signal to the actuators.

With the increasing demand for micro-scale devices, the need for improved accuracy and precision in machining processes goes up continuously. This has driven research in the development of a machine tool structure that contains the dynamic stiffness properties to machine with nano-scale accuracy and precision. One way to achieve this goal is the Tetraform, which was originally designed by Kevin Lindsey [1] at the UK's National Physical Laboratory. In his research he developed the Tetraform 1 for grinding of optical lenses with ultra smooth surfaces.

The Tetraform consists of four equilateral triangles connected by spherical masses at the vertices, which is ideal for a machining structure due to how vibration waves propagate through the structure. The vibrations travel through the closed loops of the space frame creating high dynamic stiffness with the companion of high static stiffness [2].

In this study, the Tetraform is adopted for use in micro-machining by Dr. Mark Jackson [3], where the frame has been scaled down significantly and a spindle holder in the center of the structure was added in. The modified Tetraform is used to hold a high speed spindle while the

work piece is moved with three linear position stages for two horizontal degrees of freedom and a vertical degree of freedom. The complete setup is shown in Figure 1.

Figure 1-1 Tetraform Space Frame

The structural dynamics of the Tetraform were thoroughly analyzed to compare structural modifications and to help develop and simulate active vibration control schemes. Modal analysis consists of obtaining mode shapes, natural frequencies, and damping values. The mode shapes show the displaced structure for each natural frequency. This gives insight into where areas of high vibration energy occur in the structure for different natural frequencies. The ultimate goal is to minimize modes with high energy influence on the spindle position, which create mal effects on the machining process. The Finite Element Analysis (FEA) software, ANSYS, was used to calculate and display the modal responses of the Tetraform. This software is an effective way of displaying the mode shapes along with visualizing the effects of structural modifications.

Dynamic responses of the Tetraform were also studied. Frequency response functions (FRFs) created experimentally and from simulation models show the responses of different points on the Tetraform to a dynamic input at a particular point on the Tetraform. The dynamic relationships between the spindle location and other points on the structure are of most importance. Input forces from machining can trigger certain modes of vibration when there is a strong dynamic relationship between theses two points along with the inverse affect of outer disturbance inputs creating a large dynamic response of the spindle location. Structural modifications can be conducted to strategically reduce the dynamic response between different points on the Tetraform. Dynamic analysis is also useful for the application of active vibration control. Locations of actuator-sensor pairs are critical to the effectiveness of the vibration control scheme. It is desirable to place the actuators at a point the high influence on the dynamic response of the spindle location while minimizing the dynamic response of the sensors to inputs from modes that do not significantly affect the spindle. FRFs obtained experimentally are also used to verify the simulation models created in Matlab and ANSYS.

Active vibration control via piezoelectric transducer patches is used to dampen out the critical modes which have high influence on the spindle location. Piezoelectric materials generate an electric potential from an applied mechanical stress. They also exhibit the inverse effect of expanding when subjected to an applied voltage. The development of ceramics that possess very strong mechanical electrical coupling properties is one of the driving factors behind the emergence of active vibration control as a more viable solution to vibration than passive control techniques.

These piezoelectric patches, shown in Figure 1-2, can be used as both actuators and sensors. It is beneficial to use the piezoelectric sensor to measure the strain because it is a passive sensor, as opposed to the alternative, strain gauge sensors, which require power and a Wheatstone Bridge. Sensors convert the surface strain vibration waves into an electric signal which is sent to the controller. The control algorithm is programmed onto the controller which runs in real-time. For this research, Positive Position Feedback (PPF) is chosen for its desirable stability characteristics and effective damping of multiple modes. The output control signals are input to high power amplifiers, which drive the actuators.
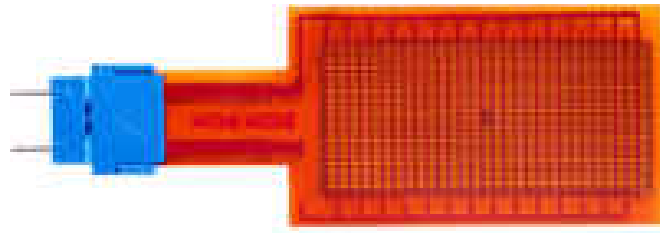
Figure 1-2 Piezoelectric Actuator/Sensor from Mide [20]

The actuators and sensor patches are mounted opposite each other on the tubular beams of the Tetraform. This allows for the assumption of collocation, which is essential for control robustness and for significant decibel reduction of critical frequencies. Optimal locations of the actuator-sensor pairs were determined from the simulation models. The mode shapes from ANSYS were used to locate areas of large displacements for the critical modes. Locations of large surface strain due to beam bending displacements are the most efficient locations for

mounting the actuators. FRFs were setup to display the dynamic relationships between the surface strain at possible mounting locations and the spindle point.

Simulations, using the Matlab FEA model, were conducted to design multiple PPF controllers and test their controllability over the targeted modes. The FEA model was converted to state space to allow for output and input matrices. Piezoelectric sensor and actuator equations were derived and input into these output and input matrices. Three piezoelectric actuator-sensor pairs were positioned at symmetric locations on the Tetraform. Different locations were tested for their controllability and required control effort. In order to dampen out modes of the Tetraform, root locus was used to tune second order PPF filters to optimal damping and stability. The effectiveness of the controllers are displayed by decibel reduction of the critical frequencies in the bode plots.

2 CHAPTER 2 – BACKGROUND

2.1 <u>Tetraform</u>

The first prototype of the Tetraform was the Tetraform 1, created by Lindsey [1] for grinding glass and quartz to optical quality at high material removal rates. With the Tetraform 1, 10 μm cuts were able to produce 5nm Ra surface finish. This model consisted of steel tubular members that were 600 mm long with an outside diameter of 131 mm. The Tetraform concept has inherently desirable dynamic characteristics. Internal damping was included for the Tetraform to further increase it's resistance to vibration. Pistons were inserted into the inner diameter of the tubular members with viscous damping material in the gaps for damping. The legs were attached to the spheres with pin joints that could be tightened or loosened to change the magnitude of the resonant frequencies. By loosening the joints, frictional damping by the pin joints became effective [1]. This along with the internal damping and dynamic stiffness properties of the frame made the Tetraform 1 highly resistant to vibration across a wide range of frequencies.

The Tetraform 1 was limited to one degree of freedom for grinding. The z-axis was on the inner portion of the structure, attached under the top sphere. It was clear that development of multi-axis machines with high stiffness were possible using the Tetraform concept. The Tetraform 'C' [13] was created adding in the two horizontal degrees of freedom. It was also determined that the pin jointed Tetraform frame had sufficient damping properties and the hydraulic damping was omitted for the Tetraform 'C' [14].

Figure 2-1 Tetraform 'C' [13]

The Tetraform concept has recently been adapted by Dr. Mark Jackson [3] at Purdue University to a smaller scale for use in micro-scale milling. The degrees of freedom needed for the machining can be implemented by linear stages mounted to the base surface, eliminating the extra mass and complexity added to the Tetraform and allowing the size of the frame to be scaled down. The pros and cons of two different models are currently being researched for the micro-milling application. Full scale and 2/3 scale models are both being built. The full scale Tetraform was shown in Figure 1-1 and a model of the 2/3 scale Tetraform is shown in Figure 2-2. The 2/3 scale model is minus some of the lower brackets and the spindle holder is also raised to a higher location in proportion of the structure.
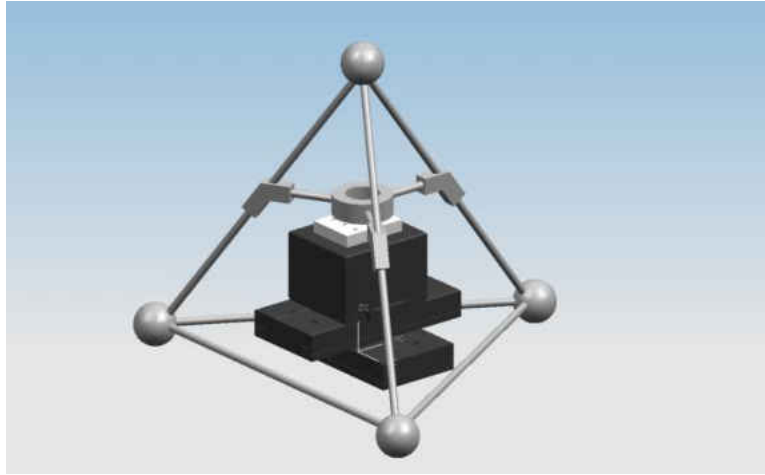
Figure 2-2 Solid Model of 2/3 Scale Tetraform

2.2   Vibration Control

Vibration control methods consist of passive control, active control, or hybrid combinations of both. Some of the most common passive damping solutions are fluid damping, viscoelastic materials, and tuned mass dampers. Active damping is most often implemented by piezoelectric materials when possible, but also could use controlled magnetism, shape memory alloys, and voice coil actuators among others. This research was only concerned with active vibration control using piezoelectric patches.

Positive Position Feedback control was chosen as the method to control the input to the piezoelectric actuators. The idea of PPF controllers was first put forth by Goh and Caughey [15]. Fanson and Caughey [8] discovered that the PPF controllers act as a low pass filter, rolling off after the controller's natural frequency, eliminating the effects of higher unmodeled modes on

the controller's output. Therefore, the controlled system will not become destabilized due to the unmodeled modes. Although PPF control guarantees robustness against the spillover of higher modes, it does not guarantee absolute stability. Conditions for the controller constants to guarantee stability can be derived by requiring the closed loop stiffness matrix to be positive definite [16]. Poh and Baz [17] modified the PPF concept to a controller which they named Modal Positive Position Feedback (MPPF). They used first order filters to obtain similar damping results as PPF filters. However, using first order filters allows lower modes to have higher influence on the control signal than the targeted mode, causing spillover effects from lower modes [16].

3   CHAPTER 3 – TETRAFORM MODELING

3.1   <u>Introduction</u>

Different models of the Tetraform were created using Finite Element Analysis (FEA). FEA is the process of breaking a complex object under analysis into smaller simpler elements in order to derive a series of equations to accurately describe it. Discretizing the object into elements allows the ability to approximate values at connecting points, or nodes. The elements that connect the different nodes use interpolation functions to approximate the relationship between the values at those nodes. In the case of structural analysis, the values being approximated are the physical displacements.   Reducing the size and therefore increasing the quantity of the elements will reduce the errors produced from using approximation functions. However, it should be noted that the size need only be reduced so much as the error will converge to zero. Further reduction is unnecessary and could even induce calculation error.

Different types of elements can be used to approximate displacements of a structure. The basic structural elements include solid, shell, plate, beam, link, and point elements. Solid elements, which are most commonly tetrahedral and brick elements, are used to mesh volumes. These are usually used when other elements are not feasible due to a large quantity of required nodes and hence a longer computing time.   Shell and plate elements are surface elements with thickness used to mesh curved or flat surfaces and can allow for bending and membrane displacements. Beam elements are used for objects whose length is larger than its other two dimensions. It's most dominant displacement is beam bending but beam elements may also

include axial and torsional displacements. Link elements are line elements that act as a spring with either axial or torsional displacements. And finally point elements are used to represent mass or inertia at one node. There are many types of these elements as there are varying theories and combinations of the different elements.

The derived element equations are in matrix form which contains mass and stiffness matrices. All of the element matrices are combined to create global mass and stiffness matrices to represent the entire structure. Both are symmetric n x n matrices where n is the total number of degrees of freedom for the entire structure. The constructed global mass and stiffness matrices are then used in a second order differential equation to describe the dynamics of the structure.

The derived FEA models of the Tetraform can then be used for modal analysis, dynamic analysis, and controller design simulations. The models were created both manually in Matlab and also in the FEA software ANSYS. The model in ANSYS was used in the modal analysis to display the mode shapes. Both were used to compare structural changes and different scales of the Tetraform. The Matlab model was used to create a state space model to be controlled for vibration control simulations.

3.2   ANSYS Finite Element Model

FEA software is a very powerful tool in the design and simulation process. In addition to the numerical solver, the modeling and results may be monitored visually. This has cut the time down significantly of today's design processes by eliminating the need for excessive

prototyping. Static stresses and dynamic characteristics can now be analyzed without the creation of entirely new prototypes. This software allows for quick and easy implementation of structural changes. Addition of structural members and changes to existing members can be done with ease while being able to visualize the resulting changes in stress and dynamic characteristics.

For this research, ANSYS 11.0 was used. When using this software, and most other FEA software, there are three steps in the analysis process. These are preprocessing, solution, and postprocessing. For the preprocessing, the model is created, meshed and the boundary conditions and input forces are applied. The solution involves defining and setting up the solver. Postprocessing is where listing and displaying of the results takes place. ANSYS combines all three into a graphical user interface environment.

Preprocessing is the first step in the analysis process. This involves the creation of the structural geometry in ANSYS. Beam elements were chosen to model the Tetraform. It is well suited for this due to its slender tubular frame without any solid volumes consisting of any significant stresses. It was assumed that the solid spheres at four outer joints and the spindle holder could be accurately represented as point masses since the internal displacements of the volumes are negligible compared to the bending of the tubular frame. It was also assumed that the bracketed sections could be modeled as thick beam sections.

Depending on the complexity of the object under analysis, it is often created in modeling software and imported into the Finite Element Software. Since the beam elements that were used are line elements, the structure was modeled in ANSYS directly as a simple wire frame.

Keypoints were used to create the basic geometry. Each keypoint's coordinates were input manually and were placed at all the points that represent a change in element orientation or cross-section. The keypoints are then connected with lines to give a wire frame representing the Tetraform. Figure 3-1 shows this wire frame before element meshing.
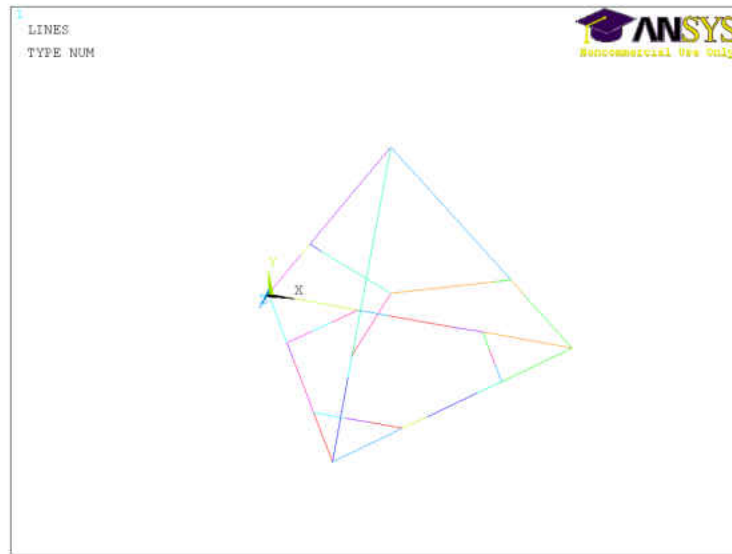
Figure 3-1 ANSYS Wire Frame Model

As can be seen from Figure 3-1, the spheres and the spindle holder are not represented in this model. They will be represented as mass elements. It is very beneficial in Finite Element Analysis to simplify the model as much as possible without affecting the results. Different FEA software packages have different limits to the allowable quantity of nodes and solution time may become excessive with larger quantities of nodes. To reduce the model, the legs of the structure were represented with beam elements while the spheres and spindle holder were represented with point mass elements. The elements used for the point masses are Mass21 elements. These are

purely inertial elements and do not affect the stiffness of the structure. This means that the input for these elements will consist of linear inertia terms, $m_x, m_y,$ and m_z, and rotational inertia terms, $I_{xx}, I_{yy},$ and I_{zz}. The three linear inertia terms are the same and are equal to the mass of the element. The rotational inertia terms, or mass moments of inertia, were found by solving (3.1) for each axis. The inertia terms for the sphere and spindle holder are listed in Table 3-1 where z is the vertical axis and x and y are the horizontal axis.

$$I = \int r^2 dm \qquad\qquad (3.1)$$

Table 3-1 Point Mass Inertia Values

	m (kg)	I_{xx} $(kg - m^2)$	I_{yy} $(kg - m^2)$	I_{zz} $(kg - m^2)$
Spheres	2.6	2.153e-3	2.153e-3	2.153e-3
Spindle Holder	1.7	1.485e-3	1.485e-3	2.225e-3

The beam elements that were used are Beam188 elements. These are used to represent slender beam structures. They are based on Timoshenko beam theory which includes shear deformation. Beam188 elements consist of two end nodes, I and J, with a total of 12 degrees of freedom. The degrees of freedom include translation on the x, y and z axes and rotation about the x, y and z axes for both end nodes. Figure 3-2 shows the orientation of this element where x, y and z are the local element coordinates and X, Y and Z are the global coordinates. A third

orientation node, J, is also included when the z direction needs to be specified. This is the case when the cross-section is not circular. This node is input to define the IJK plane.
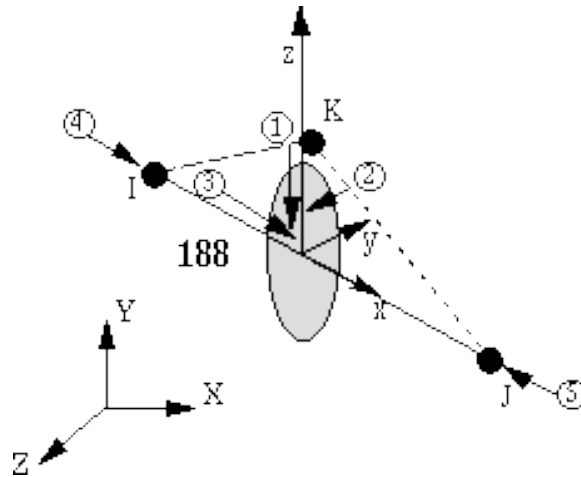
Figure 3-2 Beam188 Element [19]

Other input data for the beam elements include material properties and cross-sectional data. For this structure, there are four different beam cross-sections that need to be defined. The first is the tubular beam section and the other three are the different bracketed sections. ANSYS has options for common cross-sections where only dimensions need to be input. For uncommon cross-sections, the area moments of inertia, polar moment of inertia, and area must be input. A tubular cross-section is a common cross-section in ANSYS so the outer and inner radii are the only required input. The inner and outer radii of the legs are $R_i = \#$ and $R_o = \#$ respectively. The area, area moments of inertia, and polar moment of inertia are then calculated by ANSYS. For the bracketed sections, the area moments inertia, I_y and I_z, were calculated from the moment of a rectangular cross-section minus the moment of the circular area inside the tubular

16

beam. The polar moment of inertia J is the summation of I_y and I_z. The three bracketed cross-sections are labeled in Figure 3-3 while the calculated moments of inertia are listed in Tables 3-2 to 3-4. The Tetraform is made of steel and the material properties are listed in Table 3-5.

Figure 3-3 Bracketed Cross-Sections

Table 3-2 Bracketed Beam Cross-Section 1 Properties

Area A (m^2)	I_y (m^4)	I_z (m^4)	J (m^4)
1.799e-3	2.502e-7	3.788e-7	6.289e-7

Table 3-3 Bracketed Beam Cross-Section 2 Properties

Area A (m^2)	I_y (m^4)	I_z (m^4)	J (m^4)
1.17e-3	2.191e-7	3.624e-7	5.816e-7

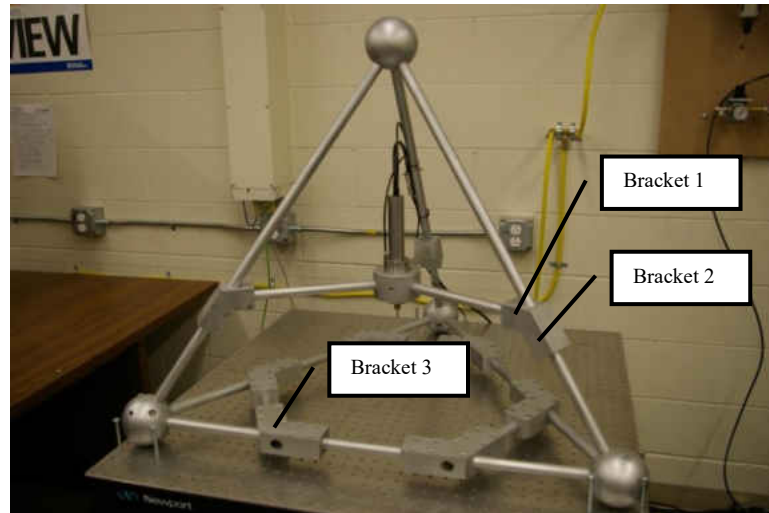Table 3-4 Bracketed Beam Cross-Section 3 Properties

Area A (m^2)	I_y (m^4)	I_z (m^4)	J (m^4)
1.813e-3	2.333e-7	4.174e-7	6.5073e-7

Table 3-5 Tetraform Material Properties

Density ρ $(\frac{kg}{m^3})$	Young's Modulus E $(\frac{N}{m^2})$	Poison's ratio v	Shear Modulus G $(\frac{N}{m^2})$
7750	207e9	0.3	79e9

The next step in the modeling process is to mesh the structure. The element length needs to be defined. For the bracketed sections, the element lengths were set to the length of the brackets. This section was not separated into multiple elements to avoid losing the slenderness ratio necessary for beam behavior. The reference node was used for this cross-section.

Finally, the boundary conditions must be defined. These were applied to the three spheres at the base of the Tetraform. The nodes at these points were restrained to zero displacement in all three translational directions. The three rotational degrees of freedom at these points were still allowed to permit transfer of vibrational energy in the lower portion of the structure. It was assumed that the weight of the Tetraform is enough to keep permanent contact with the base surface and eliminate vertical displacements of the three spheres. It is also assumed that the friction between the three spheres and the base surface are enough to eliminate horizontal movements of the spheres.

3.3   Matlab Finite Element Model

A derived Finite Element model was also created by manually coding the model in Matlab. This mathematical model serves several purposes. This FEA model was used to verify the ANSYS model by comparison of the calculated natural frequencies. It can be used to quickly implement small structural changes. Some changes are easier and quicker to change in code as opposed to making the changes in the ANSYS model. It was also used, along with the addition of the piezoelectric coupled equations, to develop a state space model that could be used for simulating the active vibration control of the Tetraform. This state space model has an input of voltage to the three piezoelectric actuators and an output of voltage from the three piezoelectric sensors. The state space model was also used to calculate the FRFs in Matlab.

The same modeling techniques used in ANSYS were used here. The frame legs were represented as Timoshenko beam elements and the spheres and spindle holder were represented as point mass elements. The same boundary conditions were applied to the three base spheres. The elements lengths were different from those of the ANSYS model. As the input data needed to be set up for each element individually, the element lengths were made larger to give fewer elements. Also, the element lengths in the area of the mounted piezoelectric sensors and actuators were setup based on optimal placement of these transducers for vibration control.

Using the element interpolation functions that approximate the displacement values across the element, equations of motion were developed to approximate the displacement values at the connecting nodes. The resulting element mass and stiffness matrices are input into the differential equation to describe the nodal displacements. The differential equation is of the form

shown in (3.2). $[M_e]$ is the element mass matrix, $[K_e]$ is the element stiffness matrix, $\{f_e\}$ is the nodal force vector, and $\{r\}$ is the nodal displacement vector.

$$[M_e]\{\ddot{r}\} + [K_e]\{r\} = \{f_e\} \tag{3.2}$$

The process of finite element analysis is to ultimately obtain global mass and stiffness matrices to represent the entire system. First, the mass and stiffness matrices are derived for each element in local coordinates (x,y,z). The mass and stiffness matrices are then converted to the global coordinate system (X,Y,Z). Finally, all the element matrices are input into the global mass and stiffness matrices that represent the entire structure. These can be used in a differential equation similar to that of (3.2).

3.3.1 Element Modeling

The element equations used for the legs were not restricted to beam theory. They also include axial and torsional displacements. The dynamic equation matrices for bending, axial and torsional movements are derived independently and superimposed into the final element matrices. These equations can be uncoupled and still represent an accurate assumption as long as large deformations do not occur. Each beam element contains twelve degrees of freedom. These include translational displacements, $u, v,$ and w, in the x, y and z directions for both nodes i and j and rotational displacements, $\theta_x, \theta_y,$ and θ_z, about the x, y and z axis for both nodes i and j. The beam element displacement vector is represented as $r^T = \{u_i, \ v_i, \ w_i, \ \theta_{xi}, \ \theta_{yi}, \ \theta_{zi}, \ u_j,$ $v_j, \ w_j, \ \theta_{xj}, \ \theta_{yj}, \ \theta_{zj}\}$.

The beam or bending equations were developed for transverse displacements, v and w. However, the derivation will just be shown for the transverse displacement w, or bending about the y axis. As in the ANSYS analysis, Timoshenko beam theory is used for the beam elements. Timoshenko beam theory differs from classical beam theory in that it includes bending shear and rotational inertia. The equations of motion for the Timoshenko beam elements for bending about the y axis will be of the form

$$[M_b]\begin{Bmatrix} \ddot{w}_i \\ \ddot{\theta}_{yi} \\ \ddot{w}_j \\ \ddot{\theta}_{yj} \end{Bmatrix} + [K_b]\begin{Bmatrix} w_i \\ \theta_{yi} \\ w_j \\ \theta_{yj} \end{Bmatrix} = \begin{Bmatrix} Q_{zi} \\ M_{yi} \\ Q_{zj} \\ M_{yj} \end{Bmatrix} \tag{3.3}$$

where $[M_b]$ is the Timoshenko beam mass matrix, $[K_b]$ is the Timoshenko beam stiffness matrix, Q_z is the nodal shear force, and M_y is the nodal bending moment about the y axis.

Hamilton's Principle will be used to derive the Timoshenko equations of motion. This principle is the variational equation listed in (3.4). The strain energy, U, kinetic energy, T, and work due to external forces, W, are derived and input into this equation to obtain the Timoshenko beam equations. The axial and transverse displacements used to derive these terms are approximated by (3.5) and (3.6) respectively. $\theta(x, t)$ is the cross-section rotation about the y axis and $\beta(x)$ is the slope due to shear.

$$\int(\delta U - \delta T - \delta W)dt = 0 \tag{3.4}$$

$$u(x, y, z, t) = z\theta(x, t) = z\left(\frac{\partial w}{\partial x} - \beta(x)\right) \tag{3.5}$$

$$w(x, y, z, t) = w(x, t) \tag{3.6}$$

As can be seen from the axial displacement, $u(x, y, z, t)$, the total slope, $\theta(x, t)$, of the cross-section is determined by the slope from bending, $\frac{\partial w}{\partial x}$, and the slope from shear, $\beta(x)$. This is one of the aspects that differentiate Timoshenko beam elements from Euler-Bernoulli beam elements. The latter does not account for shear and assumes that the beam cross-section remains perpendicular to the neutral axis. These displacements are then used to obtain the energy variation terms for Hamilton's Principle equation. The strain energy, U, and kinetic energy, T, are shown in Eqs. (3.7) and (3.8) respectively. The strain energy accounts for both linear and shear strain. These are then converted to matrix form and are given in Eqs. (3.9) and (3.10).

$$U = \frac{1}{2} E I_y \left(\frac{\partial \theta_y}{\partial x} \right)^2 + \frac{1}{2} K G A \left(\frac{\partial w}{\partial x} + \theta_y \right)^2 \tag{3.7}$$

$$T = \frac{1}{2} \rho A \left(\frac{\partial w}{\partial t} \right)^2 + \frac{1}{2} \rho I_y \left(\frac{\partial \theta_y}{\partial t} \right)^2 \tag{3.8}$$

$$U = \frac{1}{2} \int_0^{L_e} \begin{Bmatrix} \frac{\partial \theta_y}{\partial x} \\ \frac{\partial w}{\partial x} + \theta_y \end{Bmatrix}^T \begin{bmatrix} E I_y & 0 \\ 0 & K G A \end{bmatrix} \begin{Bmatrix} \frac{\partial \theta_y}{\partial x} \\ \frac{\partial w}{\partial x} + \theta_y \end{Bmatrix} dx \tag{3.9}$$

$$T = \frac{1}{2} \int_0^{L_e} \begin{Bmatrix} \frac{\partial w}{\partial t} \\ \frac{\partial \theta_y}{\partial t} \end{Bmatrix}^T \begin{bmatrix} \rho A & 0 \\ 0 & \rho I_y \end{bmatrix} \begin{Bmatrix} \frac{\partial w}{\partial t} \\ \frac{\partial \theta_y}{\partial t} \end{Bmatrix} dx \tag{3.10}$$

Here, w is the transverse displacement in the z direction, θ_y is the rotation of the beam cross-section about y axis, L_e is the length of the element, A is the cross-sectional area, E is the

Modulus of Elasticity, I_y is the bending moment about the y axis, K is the shear coefficient and is most often given the value of $\frac{9}{10}$ [18], and G is the shear modulus.

The work done by external forces W is also given as

$$W = \int_0^{L_e} \begin{bmatrix} w \\ \theta_y \end{bmatrix}^T \begin{bmatrix} Q \\ M \end{bmatrix} dx \qquad (3.11)$$

where Q is the shear force and M is the bending moment.

Equations (3.9), (3.10) and (3.11) are then substituted into (3.4). The resulting equations of motion are the Timoshenko beam equations and are given in (3.12) and (3.13).

$$\frac{\partial \left\{ KGA \left(\frac{\partial w}{\partial x} + \theta_y \right) \right\}}{\partial x} + Q = \rho A \frac{\partial^2 w}{\partial t^2} \qquad (3.12)$$

$$\frac{\partial \left\{ EI \left(\frac{\partial \theta_y}{\partial x} \right) \right\}}{\partial x} - KGA \left(\frac{\partial w}{\partial x} + \theta_y \right) + M = \rho I_y \frac{\partial^2 \theta_y}{\partial t^2} \qquad (3.13)$$

From this, it can be seen that a quadratic interpolation function for w must be used. The interpolation function for θ_y can be obtained from taking the spatial derivative of w. Both of these equations for displacements are then used along with the boundary conditions listed in (3.16) and (3.17) to calculate the shape functions. The shape functions for transverse displacement, rotations and accelerations are $\{N_w\}$, $\{N_\theta\}$ and $\{N_a\}$ respectively where $\{N_\theta\} = \{N_w\}'$ and $\{N_a\} = \{N_w\}''$. $(.)'$ denotes the spatial derivative in the x direction.

$$w = a_1 + a_2 x + a_3 x^2 + a_4 x^3 \qquad (3.14)$$

$$\theta_y = w' = a_2 + 2a_3 x + 3a_4 x^2 \qquad (3.15)$$

$$w(0) = w_i, \theta_y(0) = -\theta_i \tag{3.16}$$

$$w(L_e) = w_j, \theta_y = -\theta_j \tag{3.17}$$

$$w(x,t) = \{N_w\}^T\{\varphi\} \tag{3.18}$$

$$\dot{w}(x,t) = \{N_w\}^T\{\dot{\varphi}\} \tag{3.19}$$

$$w'(x,t) = \{N_\theta\}^T\{\varphi\} \tag{3.20}$$

$$w''(x,t) = \{N_a\}^T\{\varphi\} \tag{3.21}$$

Finally, these shape functions along with the Timoshenko beam equations listed in (3.12) and (3.13) are used to obtain expressions for the stiffness matrix $[K_b]$ and the mass matrix $[M_b]$ listed in (3.22) and (3.23). Solving these expressions gives the matrices listed in (3.24) and (3.25). The first term in the mass matrix is the translational inertia and the second term is the rotational inertia.

$$[K_b] = \int_0^{L_e} \begin{bmatrix} \frac{\partial}{\partial x}[N_\theta] \\ [N_\theta] + \frac{\partial}{\partial x}[N_w] \end{bmatrix}^T \begin{bmatrix} EI_y & 0 \\ 0 & KGA \end{bmatrix} \begin{bmatrix} \frac{\partial}{\partial x}[N_\theta] \\ [N_\theta] + \frac{\partial}{\partial x}[N_w] \end{bmatrix} dx \tag{3.22}$$

$$[M_b] = \int_0^{L_e} \begin{bmatrix} N_w \\ N_\theta \end{bmatrix}^T \begin{bmatrix} \rho A & 0 \\ 0 & \rho I_y \end{bmatrix} \begin{bmatrix} N_w \\ N_\theta \end{bmatrix} dx \tag{3.23}$$

$$[K_b] = \frac{EI_y}{(1+\sigma)L_e^3} \begin{bmatrix} 12 & 6L_e & -12 & 6L_e \\ 6L_e & (4+\sigma)L_e^2 & -6L_e & (2-\sigma)L_e^2 \\ -12 & -6L_e & 12 & -6L_e \\ 6L_e & (2-\sigma)L_e^2 & -6L_e & (4+\sigma)L_e^2 \end{bmatrix} \tag{3.24}$$

$$[M_b] =$$

$$\frac{\rho A}{210(1+\sigma)^2}\begin{bmatrix} (70\sigma^2 + 147\sigma + 78) & \frac{(35\sigma^2+77\sigma+44)L_e}{4} & (35\sigma^2 + 63\sigma + 27) & -\left(\frac{(35\sigma^2+63\sigma+26)L_e}{4}\right) \\ \left(\frac{(35\sigma^2+77\sigma+44)L_e}{4}\right) & \left(\frac{(7\sigma^2+14\sigma+8)L_e^2}{4}\right) & \left(\frac{(35\sigma^2+63\sigma+26)L_e}{4}\right) & -\left(\frac{(7\sigma^2+14\sigma+6)L_e^2}{4}\right) \\ (35\sigma^2 + 63\sigma + 27) & \left(\frac{(35\sigma^2+63\sigma+26)L_e}{4}\right) & (70\sigma^2 + 147\sigma + 78) & -\left(\frac{(35\sigma^2+77\sigma+44)L_e}{4}\right) \\ -\left(\frac{(35\sigma^2+63\sigma+26)L_e}{4}\right) & -\left(\frac{(7\sigma^2+14\sigma+6)L_e^2}{4}\right) & -\left(\frac{(35\sigma^2+77\sigma+44)L_e}{4}\right) & \left(\frac{(7\sigma^2+14\sigma+8)L_e^2}{4}\right) \end{bmatrix} +$$

$$\frac{\rho I_y}{30(1+\sigma)^2 L_e}\begin{bmatrix} 36 & -(15\sigma - 3)L_e & -36 & -(15\sigma - 3)L_e \\ -(15\sigma - 3)L_e & (10\sigma^2 + 5\sigma + 4)L_e^2 & (15\sigma - 3)L_e & (5\sigma^2 - 5\sigma - 1)L_e^2 \\ -36 & (15\sigma - 3)L_e & 36 & (15\sigma - 3)L_e \\ -(15\sigma - 3)L_e & (5\sigma^2 - 5\sigma - 1)L_e^2 & (15\sigma - 3)L_e & (10\sigma^2 + 5\sigma + 4)L_e^2 \end{bmatrix}$$

$$(3.25)$$

where $\sigma = \frac{12}{L_e^2}\left(\frac{EI_y}{KAG}\right)$.

The axial and torsional equations use classical element stiffness and mass matrices. The axial equations of motion will be in the form of (3.26). The torsional equations of motion will be in the form of (3.27).

$$[M_a]\begin{Bmatrix} \ddot{u}_i \\ \ddot{u}_j \end{Bmatrix} + [K_a]\begin{Bmatrix} u_i \\ u_j \end{Bmatrix} = \begin{Bmatrix} F_{xi} \\ F_{xj} \end{Bmatrix} \tag{3.26}$$

$$[M_t]\begin{Bmatrix} \ddot{\theta}_{xi} \\ \ddot{\theta}_{xj} \end{Bmatrix} + [K_t]\begin{Bmatrix} \theta_{xi} \\ \theta_{xj} \end{Bmatrix} = \begin{Bmatrix} M_{xi} \\ M_{xj} \end{Bmatrix} \tag{3.27}$$

The axial stiffness, $[K_a]$, and mass, $[M_a]$, matrices are given in (3.28) and (3.29) and the torsional stiffness, $[K_t]$, and mass, $[M_t]$, matrices are listed in (3.30) and (3.31).

$$[K_a] = \begin{bmatrix} \dfrac{AE}{L_e} & -\dfrac{AE}{L_e} \\ -\dfrac{AE}{L_e} & \dfrac{AE}{L_e} \end{bmatrix} \quad (3.28)$$

$$[M_a] = \begin{bmatrix} \dfrac{\rho A L_e}{3} & \dfrac{\rho A L_e}{6} \\ \dfrac{\rho A L_e}{6} & \dfrac{\rho A L_e}{3} \end{bmatrix} \quad (3.29)$$

$$[K_t] = \begin{bmatrix} \dfrac{GJ}{L_e} & -\dfrac{GJ}{L_e} \\ -\dfrac{GJ}{L_e} & \dfrac{GJ}{L_e} \end{bmatrix} \quad (3.30)$$

$$[M_t] = \begin{bmatrix} \dfrac{\rho J L_e}{3} & \dfrac{\rho J L_e}{6} \\ \dfrac{\rho J L_e}{6} & \dfrac{\rho J L_e}{3} \end{bmatrix} \quad (3.31)$$

The bending, axial and torsional matrices are then input into (3.2) to give the element stiffness, $[K_e]$, and mass, $[M_e]$, matrices displayed in (3.32) and (3.33).

$[K_e]$

$$= \begin{bmatrix}
K_{a11} & 0 & 0 & 0 & 0 & 0 & K_{a12} & 0 & 0 & 0 & 0 & 0 \\
0 & K_{b11} & 0 & 0 & 0 & K_{b12} & 0 & K_{b13} & 0 & 0 & 0 & K_{b14} \\
0 & 0 & K_{b11} & 0 & -K_{b12} & 0 & 0 & 0 & K_{b13} & 0 & -K_{b14} & 0 \\
0 & 0 & 0 & K_{t11} & 0 & 0 & 0 & 0 & 0 & K_{t12} & 0 & 0 \\
0 & 0 & -K_{b12} & 0 & K_{b22} & 0 & 0 & 0 & -K_{b14} & 0 & K_{b24} & 0 \\
0 & K_{b12} & 0 & 0 & 0 & K_{b22} & 0 & K_{b14} & 0 & 0 & 0 & K_{b24} \\
K_{a12} & 0 & 0 & 0 & 0 & 0 & K_{a22} & 0 & 0 & 0 & 0 & 0 \\
0 & K_{b31} & 0 & 0 & 0 & K_{b32} & 0 & K_{b33} & 0 & 0 & 0 & K_{b34} \\
0 & 0 & K_{b31} & 0 & -K_{b32} & 0 & 0 & 0 & K_{b33} & 0 & -K_{b34} & 0 \\
0 & 0 & 0 & K_{t12} & 0 & 0 & 0 & 0 & 0 & K_{t22} & 0 & 0 \\
0 & 0 & -K_{b32} & 0 & K_{b42} & 0 & 0 & 0 & -K_{b34} & 0 & K_{b44} & 0 \\
0 & K_{b32} & 0 & 0 & 0 & K_{b42} & 0 & K_{b34} & 0 & 0 & 0 & K_{b44}
\end{bmatrix}$$

$$(3.32)$$

$$[M_e]$$

$$
= \begin{bmatrix}
M_{a11} & 0 & 0 & 0 & 0 & 0 & M_{a12} & 0 & 0 & 0 & 0 & 0 \\
0 & M_{b11} & 0 & 0 & 0 & M_{b12} & 0 & M_{b13} & 0 & 0 & 0 & M_{b14} \\
0 & 0 & M_{b11} & 0 & -M_{b12} & 0 & 0 & 0 & M_{b13} & 0 & -M_{b14} & 0 \\
0 & 0 & 0 & M_{t11} & 0 & 0 & 0 & 0 & 0 & M_{t12} & 0 & 0 \\
0 & 0 & -M_{b12} & 0 & M_{b22} & 0 & 0 & 0 & -M_{b14} & 0 & M_{b24} & 0 \\
0 & M_{b12} & 0 & 0 & 0 & M_{b22} & 0 & M_{b14} & 0 & 0 & 0 & M_{b24} \\
M_{a12} & 0 & 0 & 0 & 0 & 0 & M_{a22} & 0 & 0 & 0 & 0 & 0 \\
0 & M_{b31} & 0 & 0 & 0 & M_{b32} & 0 & M_{b33} & 0 & 0 & 0 & M_{b34} \\
0 & 0 & M_{b31} & 0 & -M_{b32} & 0 & 0 & 0 & M_{b33} & 0 & -M_{b34} & 0 \\
0 & 0 & 0 & M_{t12} & 0 & 0 & 0 & 0 & 0 & M_{t22} & 0 & 0 \\
0 & 0 & -M_{b32} & 0 & M_{b42} & 0 & 0 & 0 & -M_{b34} & 0 & M_{b44} & 0 \\
0 & M_{b32} & 0 & 0 & 0 & M_{b42} & 0 & M_{b34} & 0 & 0 & 0 & M_{b44}
\end{bmatrix}
$$

$$(3.33)$$

3.3.2 Construction of Global Matrices

Once these element matrices are calculated, they need to be converted from local to global coordinates. This is done by computing a transformation matrix, $[T]$. Matrix $[T_e]$ is made by inputting the angles between the local and global axes. This matrix is then input into $[T]$. There are four T_e terms in this matrix because there are six degrees of freedom per node or twelve per element. The element stiffness and mass matrices are then converted using Eqs. (3.36) and (3.37) where $[K_{e'}]$ is the element stiffness matrix in global coordinates and $[M_{e'}]$ is the element mass matrix in global coordinates.

.

$$[T_e] = \begin{bmatrix} \cos(\langle x,X \rangle) & \cos(\langle x,Y \rangle) & \cos(\langle x,Z \rangle) \\ \cos(\langle y,X \rangle) & \cos(\langle y,Y \rangle) & \cos(\langle y,Z \rangle) \\ \cos(\langle z,X \rangle) & \cos(\langle z,Y \rangle) & \cos(\langle z,Z \rangle) \end{bmatrix} \tag{3.34}$$

$$[T] = \begin{bmatrix} T_e & 0 & 0 & 0 \\ 0 & T_e & 0 & 0 \\ 0 & 0 & T_e & 0 \\ 0 & 0 & 0 & T_e \end{bmatrix} \tag{3.35}$$

$$[K_{e'}] = [T]^T [Ke][T] \tag{3.36}$$

$$[M_{e'}] = [T]^T [Me][T] \tag{3.37}$$

Now that the element matrices are in the global coordinates, the global matrices can be constructed. Each matrix can be broken up to the form of (3.38), where i and j are the node numbers for that particular element. Therefore, each quadrant of the matrix can be input into the global matrix at a place that corresponds to the global node numbers for the element.

$$[K_{e'}] = \begin{bmatrix} K_{ii} & K_{ij} \\ K_{ij}^T & K_{jj} \end{bmatrix} \tag{3.38}$$

The last step in creation of the model is to add the mass elements. These include four spheres and the spindle holder. Since these are point masses, the inertia terms will lie on the diagonal of the mass matrix. These point masses will have no affect on the stiffness matrix. The terms in the matrices will be the same as those calculated for the ANSYS method. These point mass matrices will be input to the global matrix where the diagonal terms correspond to that particular node. Here, m is the mass of the object and I_{xx}, I_{yy}, and I_{zz} are the mass moments of inertia.

$$[M_{pointmass}] = \begin{bmatrix} m & 0 & 0 & 0 & 0 & 0 \\ 0 & m & 0 & 0 & 0 & 0 \\ 0 & 0 & m & 0 & 0 & 0 \\ 0 & 0 & 0 & I_{xx} & 0 & 0 \\ 0 & 0 & 0 & 0 & I_{yy} & 0 \\ 0 & 0 & 0 & 0 & 0 & I_{zz} \end{bmatrix} \qquad (3.39)$$

4   CHAPTER 4 – MODAL ANALYSIS

4.1   Introduction

Modal analysis was conducted on the different Tetraform prototypes. This was done using both the ANSYS and Matlab models.   The modal analysis results are the natural frequencies and the mode shapes.   The mode shapes are the structural displacements at a particular natural frequency and are used to analyze where the areas of high energy are on the Tetraform for that natural frequency.   It is not desirable to have modes with high vibrational energy at the point of the spindle holder.   The frequencies that fall into this category are considered critical frequencies.   The mode shapes for the critical frequencies can be used to identify all of the areas of high surface strain that could be used to attach the piezoelectric sensors and actuators.   The mode shapes and frequencies for different Tetraforms are also compared to see the advantages of the different models.

4.2   Full Scale Modal Analysis Results from ANSYS

The first modal analysis results are from the full scale Tetraform. This is the Tetraform model to which active vibration will be applied to. The modal analysis method used in ANSYS was Block Lanczos. The first results obtained were for the full scale Tetraform without the spindle motor and bearing attached to the spindle holder. This additional mass and inertia is added for the second set of results. The mode shapes and frequencies for the first 12 modes are displayed in Figures 4-1 to 4-12. These mode shapes are used to analyze which modes are

critical to the machining process. The modes which contain large displacements at the center

point mass, which represents the spindle holder, are the critical modes of interest.

4.2.1   Full Scale Mode Shapes without Spindle
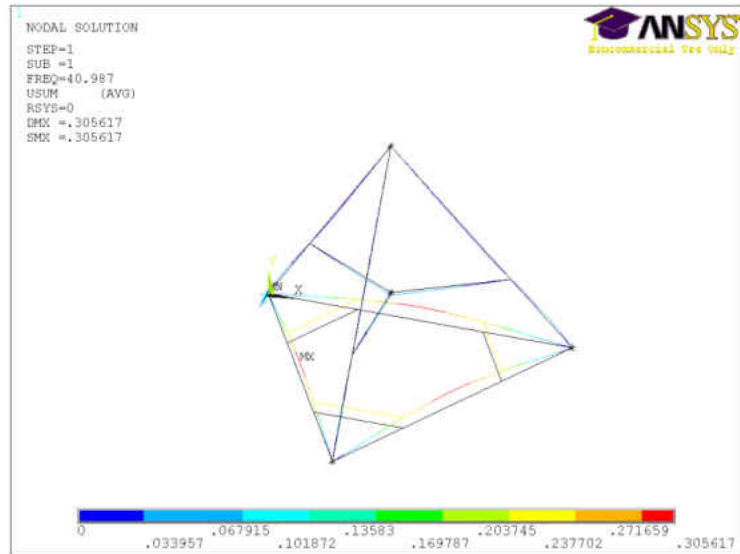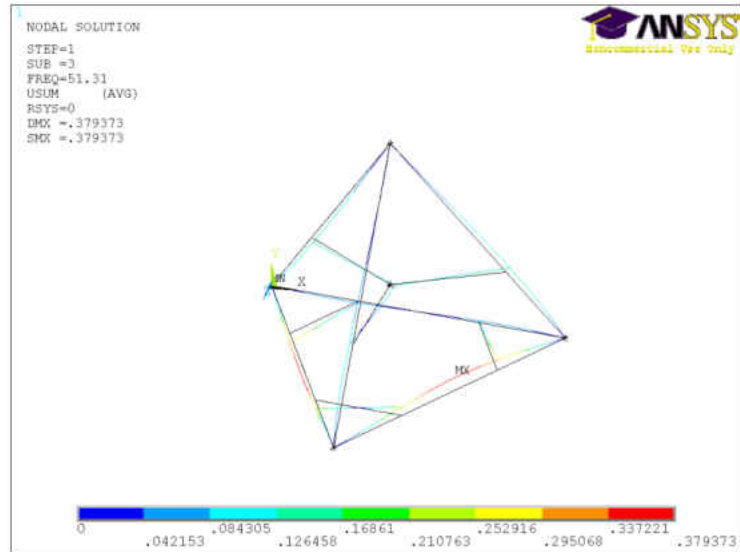

Figure 4-1 Mode 1 @41.0 Hz

Figure 4-2 Mode 2 @ 51.3 Hz

Mode 1 contains most of its energy in the lower portion of the structure. The lower beams vibrate with full length bending with the largest displacement at the middle of the beam. Some of the vibrational energy is translated to the upper portion of the structure, creating slight vertical displacement of the spindle. Mode 2 is similar in the fact that it is mostly made up of full length bending of the lower beams. It, however, creates small horizontal displacements of the spindle holder. The brackets in the lower portion of the structure apply little stiffness to these modes. This, along with the added mass of the lower brackets, keeps these frequencies in the lower end of the frequency spectrum.
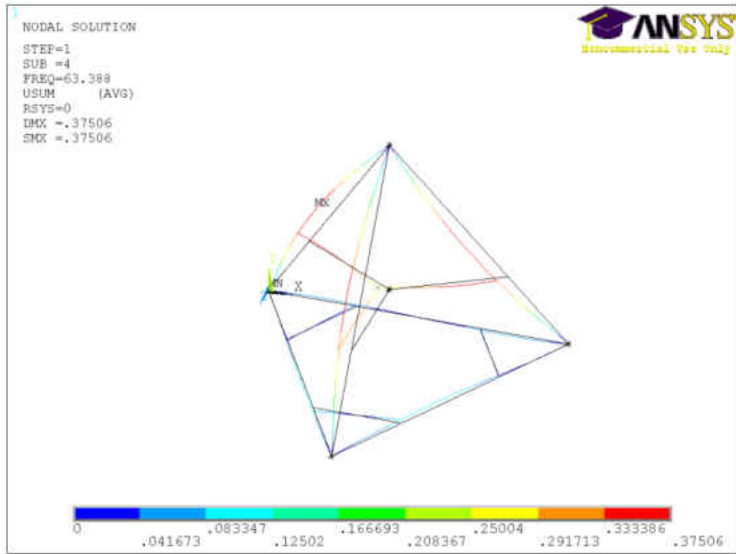
Figure 4-3 Mode 3 @ 63.4 Hz
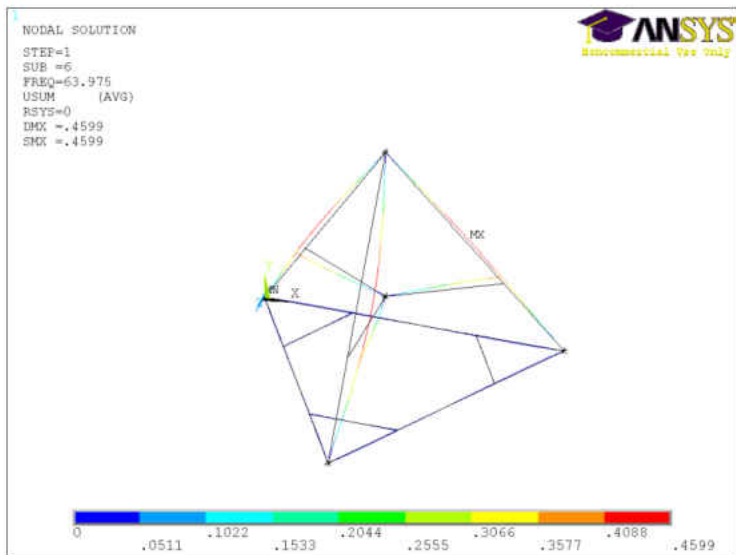
Figure 4-4 Mode 4 @64.0 Hz

Modes 3 and 4 consist of full length bending of the upper beams. The bending from Mode 3 causes the Tetraform to sway horizontally creating large horizontal displacement of the spindle holder. Mode 3 is the dominant critical mode for horizontal displacement of the spindle holder. The bending of the beams in Mode 4 causes the Tetraform to rotate about its center vertical axis. This creates only a rotational displacement about the vertical axis for the spindle holder.
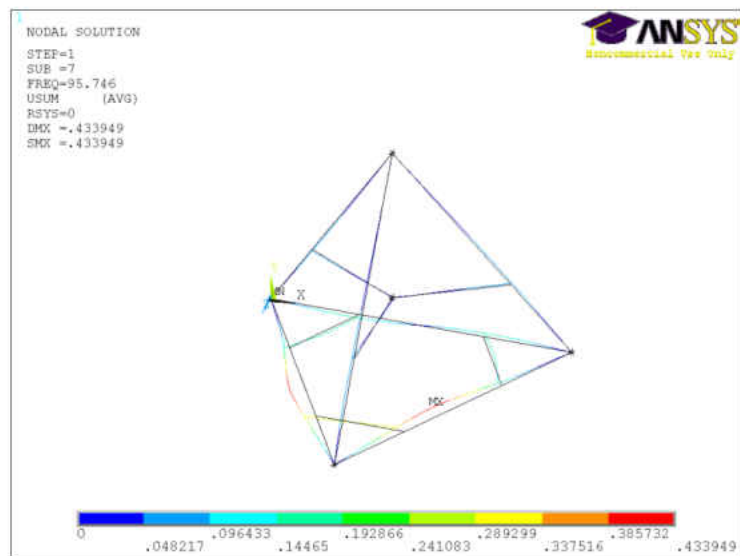
Figure 4-5 Mode 5 @ 95.7 Hz
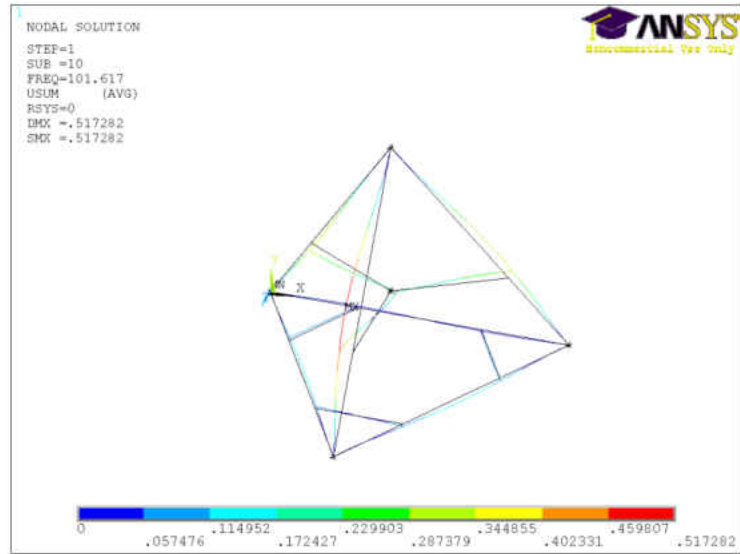
Figure 4-6 Mode 6 @ 101.6 Hz

Mode 5 contains horizontal bending of the lower beams with minimal energy translated to the rest of the structure. Mode 6 causes bending of the upper beams with small horizontal displacements of the spindle holder.
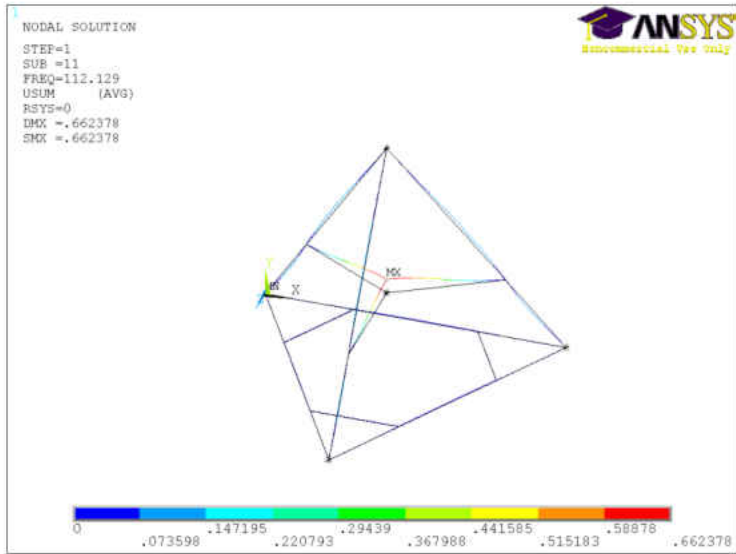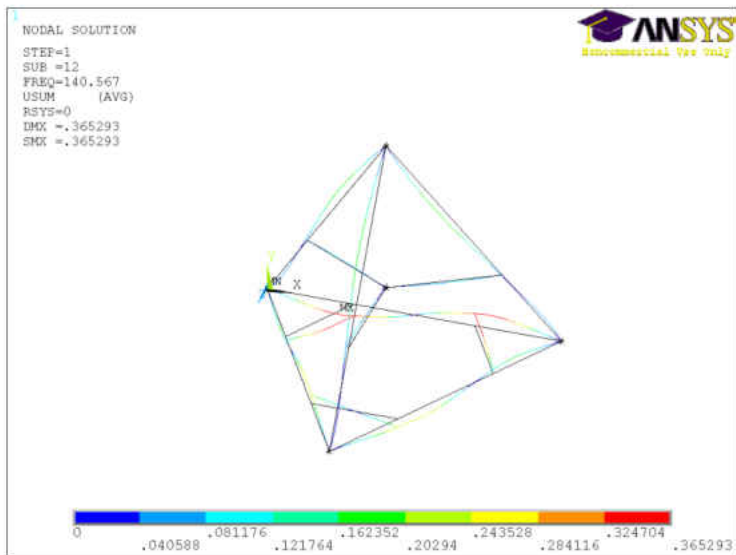
Figure 4-7 Mode 7 @ 112.1 Hz

Figure 4-8 Mode 8 @ 140.6 Hz

Mode 7 contains bending of the inner beams which attach the spindle holder, creating large vertical displacements of the spindle holder. This mode is the dominant critical mode for vertical displacement of the spindle holder. This mode is also highly sensitive to the addition of mass and inertia of different spindles attached to the holder. Mode 8 consists of energy throughout most of the structure but does not affect the inner beams attaching the spindle holder.
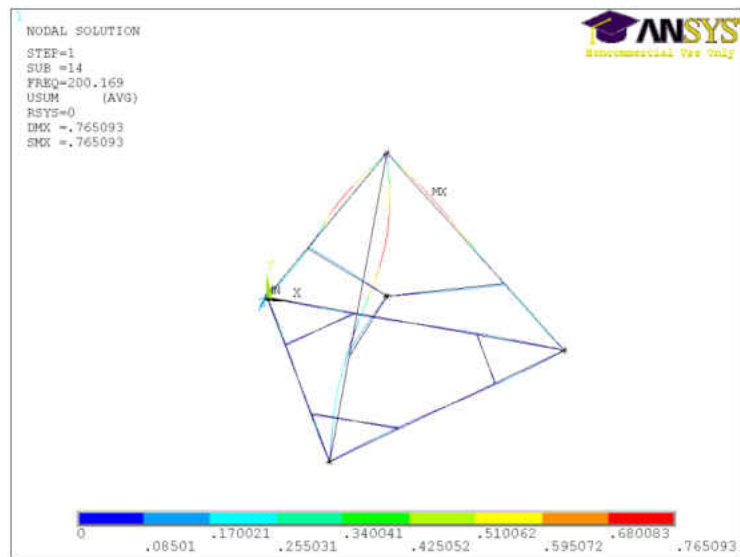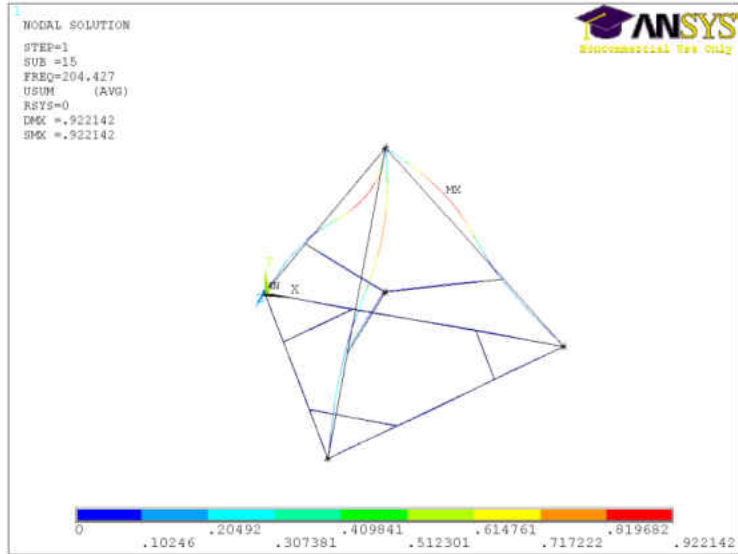

Figure 4-9 Mode 9 @ 200.2 Hz
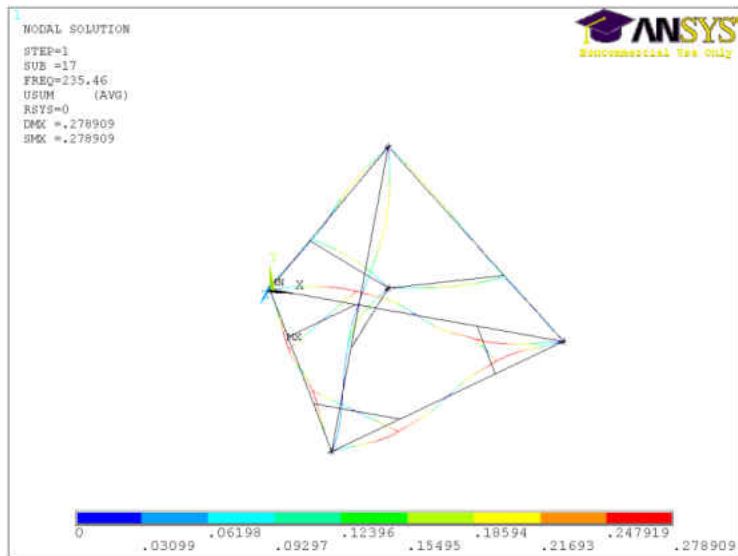
Figure 4-10 Mode 10 @ 204.4 Hz
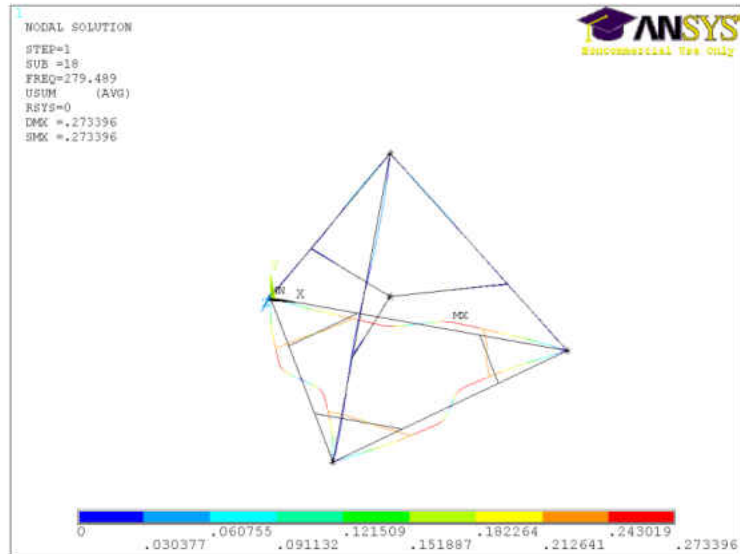

Figure 4-11 Mode 11 @ 235.5 Hz

Figure 4-12 Mode 12 @ 279.5 Hz

Modes 9 and 10 consist of bending of the top portion of the upper beams with little to no energy in the rest of the Tetraform. Mode 11 has vibration through out the structure with a wave node placed at the spindle holder. This wave node has no translational displacements. However, the spindle point has large rotational displacements. Mode 12 contains nearly all of its energy as horizontal displacements of the lower beams. Here, the bracketed sections translate as three rigid bodies.

4.2.2 Full Scale Mode Shapes with Spindle

Next, the mode shapes were obtained for the Tetraform with the spindle motor and bearing mass and inertia included. These are the mode shapes which represent the Tetraform which will be used for the active vibration control simulations. It is important to conduct a modal analysis for the Tetraform with and without the spindle. For different machining

applications, different sized spindles and spindle holders would be used. Therefore, it is important to understand how the changes in mass and inertia of this point will affect the mode shapes and frequencies. Figure 4-13 shows the spindle assembly mounted in the spindle holder.
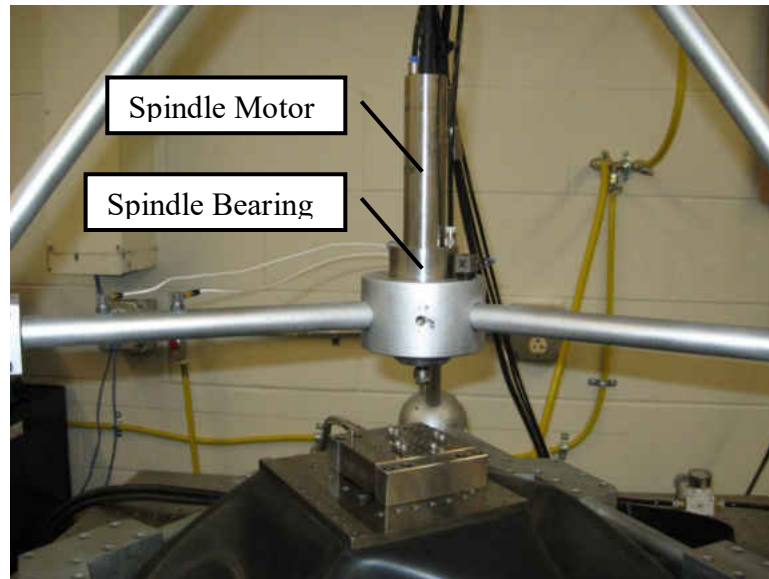

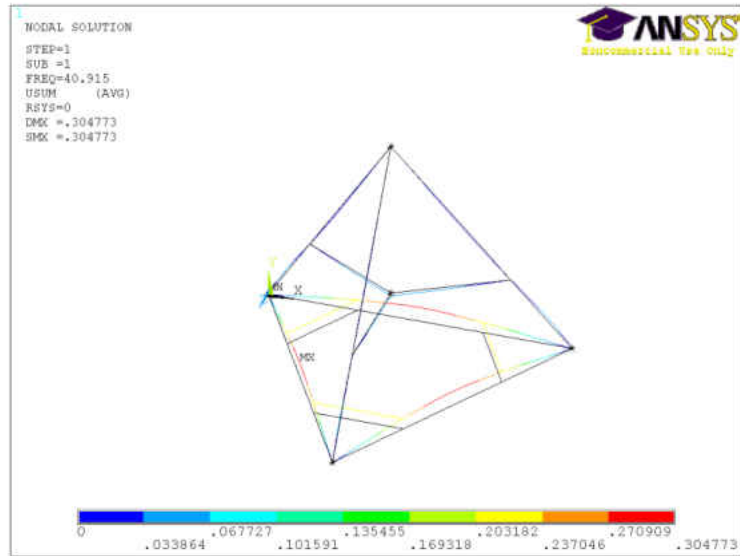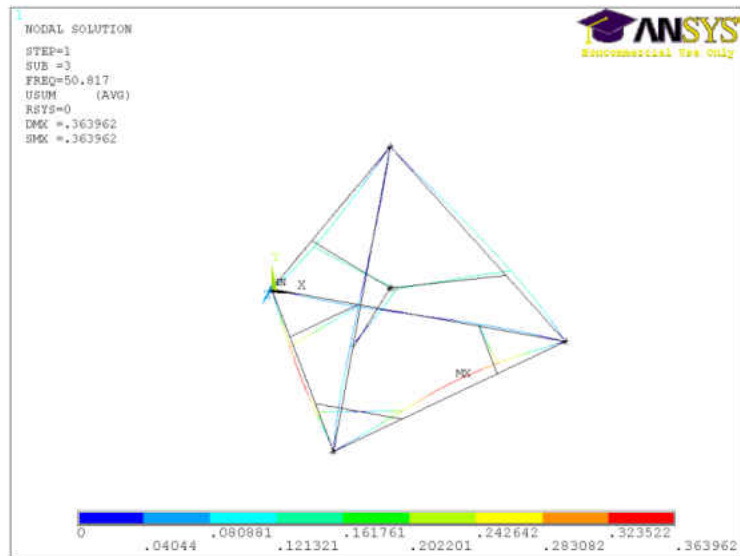Figure 4-13 Spindle Bearing and Spindle Motor

Figure 4-14 Mode 1 @ 40.9 Hz
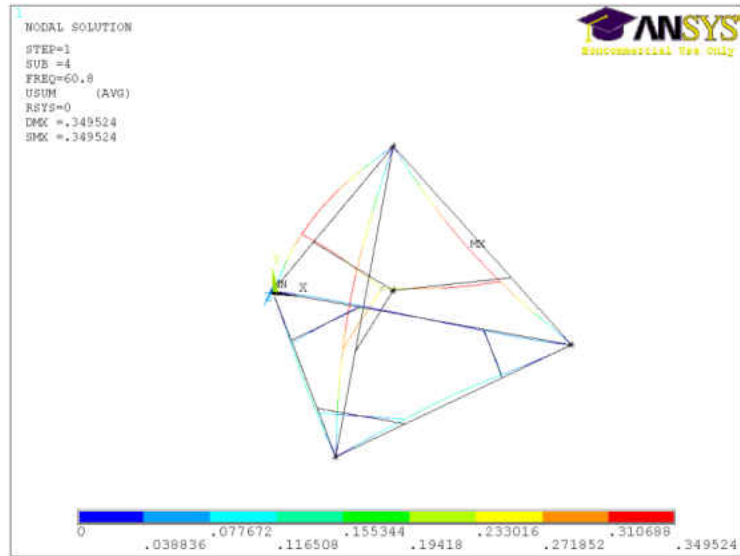

Figure 4-15 Mode 2 @ 50.8 Hz
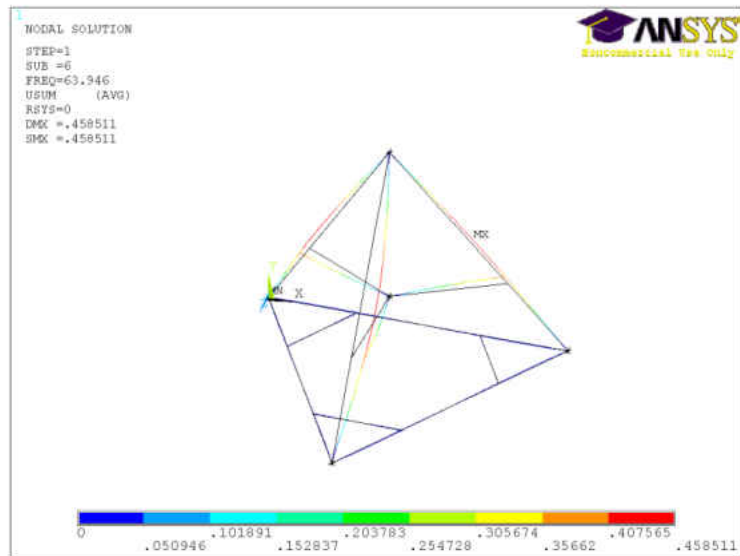
41

Figure 4-16 Mode 3 @ 60.8 Hz
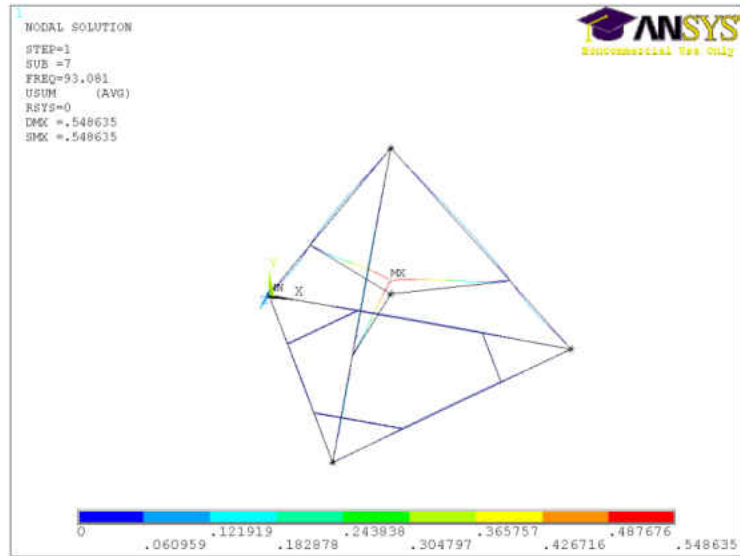

Figure 4-17 Mode 4 @ 63.95 Hz
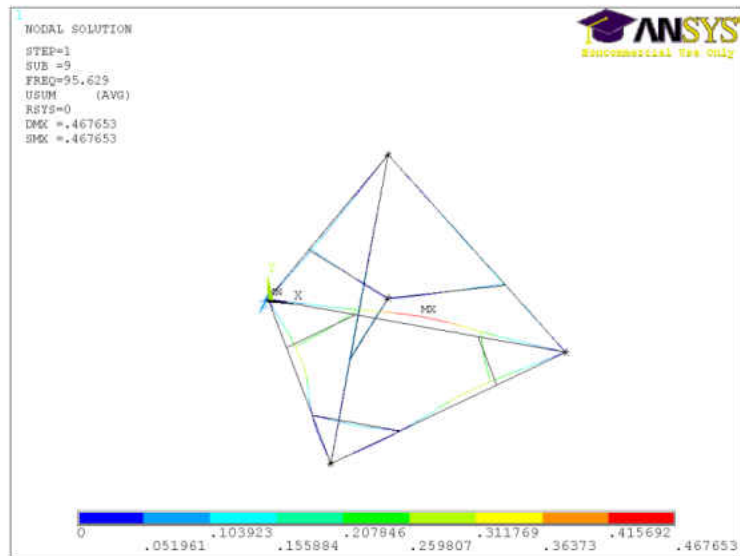
Figure 4-18 Mode 5 @ 93.1 Hz
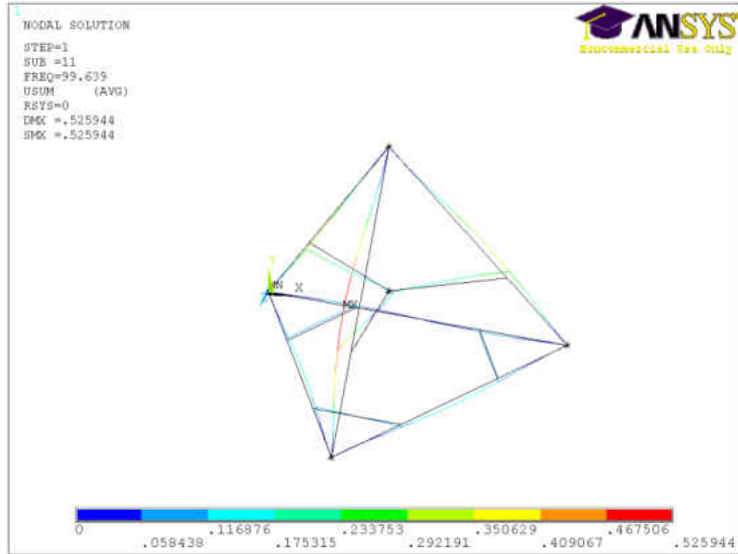

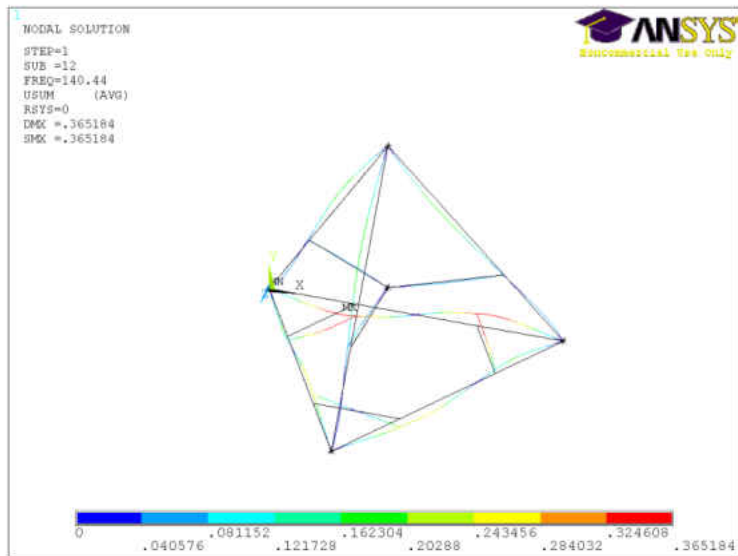Figure 4-19 Mode 6 @ 95.6 Hz

Figure 4-20 Mode 7 @ 99.6 Hz

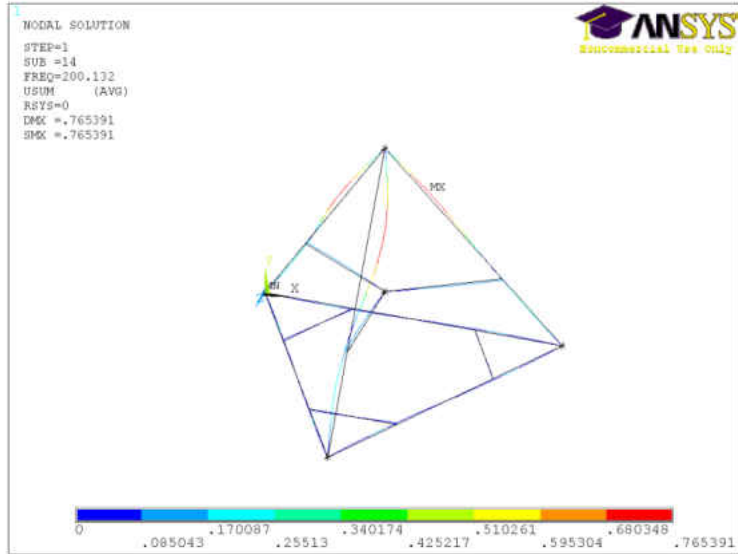Figure 4-21 Mode 8 @ 140.4 Hz

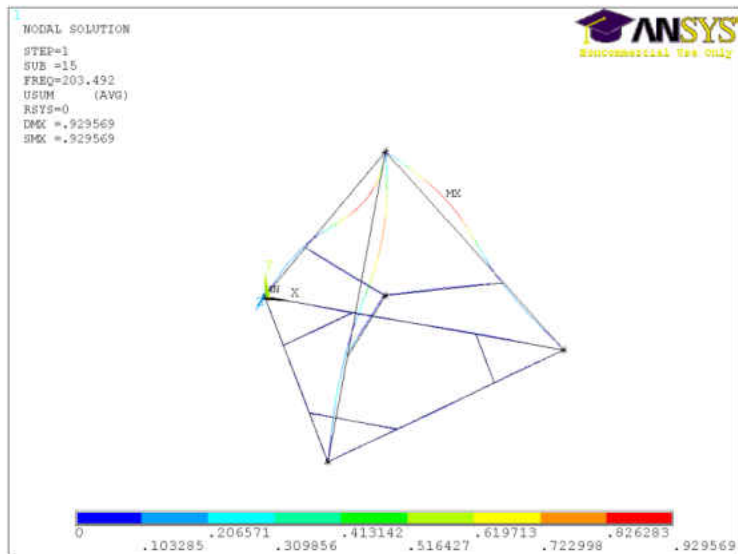Figure 4-22 Mode 9 @ 200.1 Hz

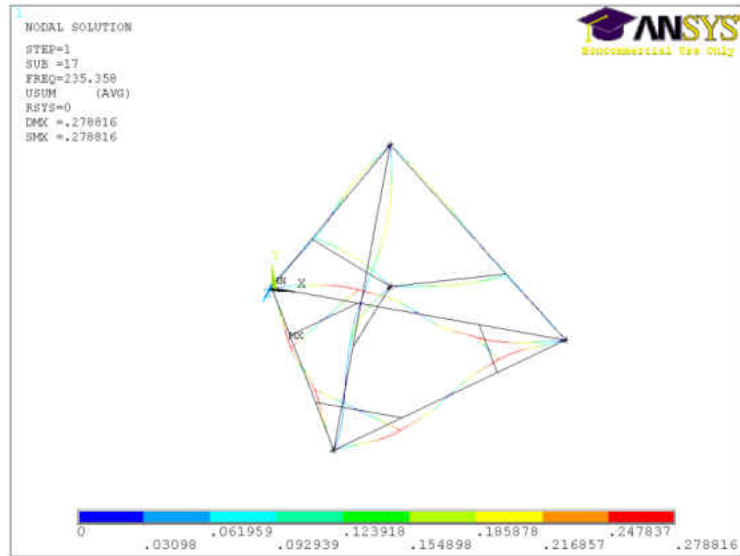Figure 4-23 Mode 10 @ 203.5 Hz
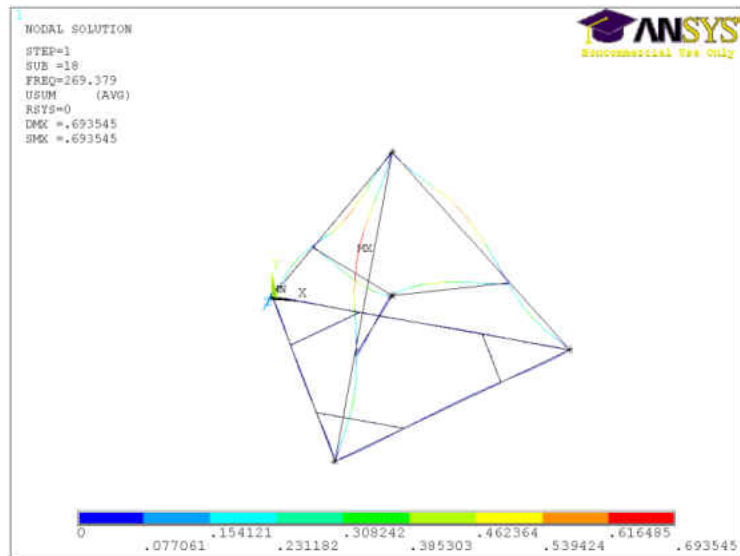
Figure 4-24 Mode 11 @ 235.4 Hz

Figure 4-25 Mode 12 @ 269.4 Hz

The added inertia from the spindle will have a greater affect on the modes with larger displacements at the spindle location. However, many of the modes contain significant moving mass throughout the structure which causes the inertia of the spindle location to be of smaller importance. For some critical modes, the modal mass is dominated by the mass of the spindle. For instance, Mode 5 with the spindle added is very sensitive to the mass at the spindle location. This mode acts similar to a large mass connected to three cantilever beams. Changing the mass in the middle has a large affect on this mode. This mode was shifted from 112.1 Hz, without the spindle, to 93.1 Hz, with the spindle. Comparison of the frequencies for the Tetraforms, with and without the spindle, is shown in Table 4-1.

Table 4-1 Full Scale Tetraform Natural Frequencies without Spindle

Mode	1st	2nd	3rd	4th	5th	6th	7th	8th	9th	10th	11th	12th
No Spindle (Hz)	41.0	51.3	63.4	64.0	95.7	101.6	112.1	140.6	200.2	204.4	235.5	279.5
Spindle Added (Hz)	40.9	50.8	60.8	64.0	93.1	95.6	99.6	140.4	200.1	203.5	235.4	269.4

4.2.3　Full Scale Mode Shapes without Lower Brackets

The Tetraform was also analyzed without the lower brackets. Depending upon the machining application, it may be needed to remove the lower brackets to create more room for the linear stages which move the workpiece. Therefore, the effects of removing these brackets were important to be investigated.
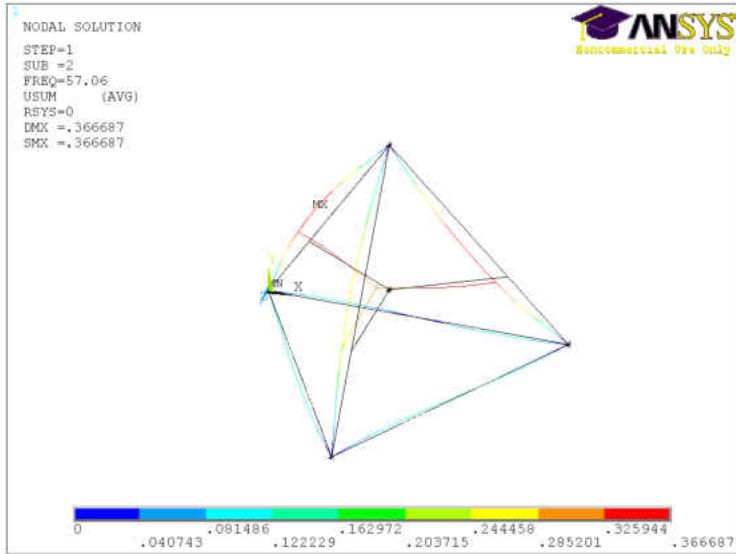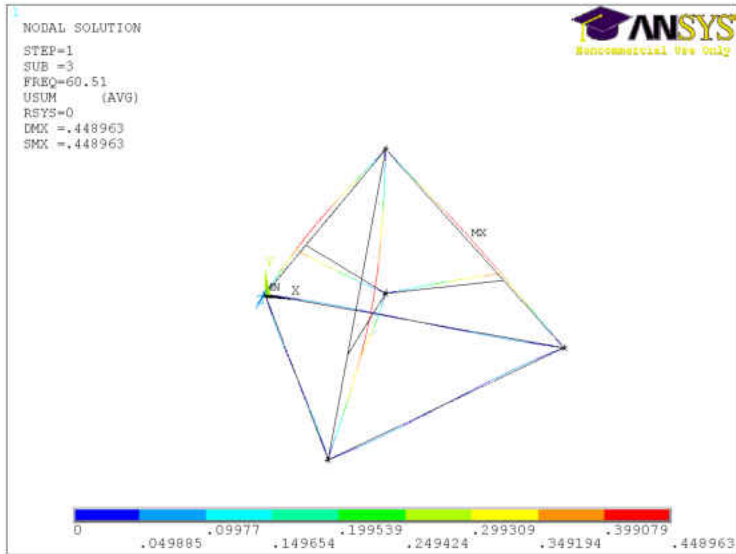
Figure 4-26 Mode 1 @ 57.1 Hz
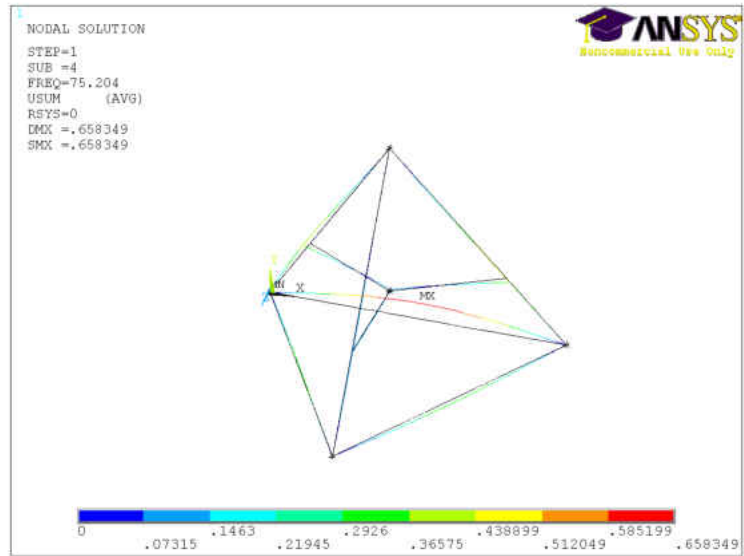

Figure 4-27 Mode 2 @ 60.5 Hz

Figure 4-28 Mode 3 @ 75.2 Hz
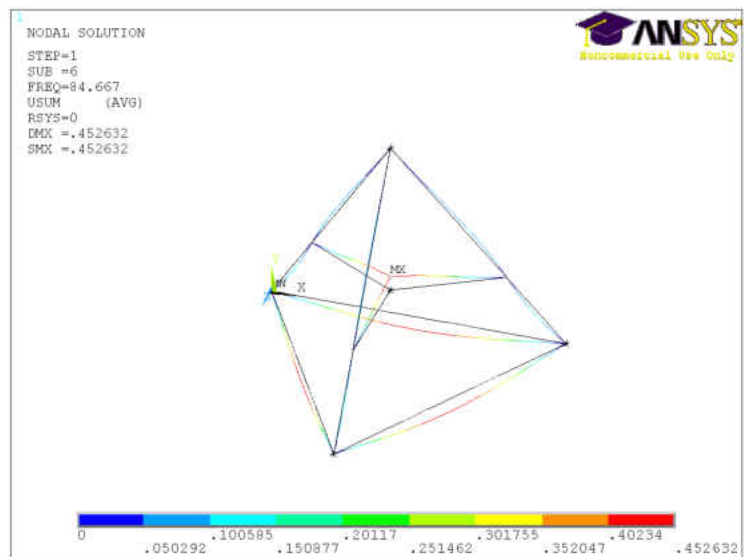
Figure 4-29 Mode 4 @ 84.7 Hz
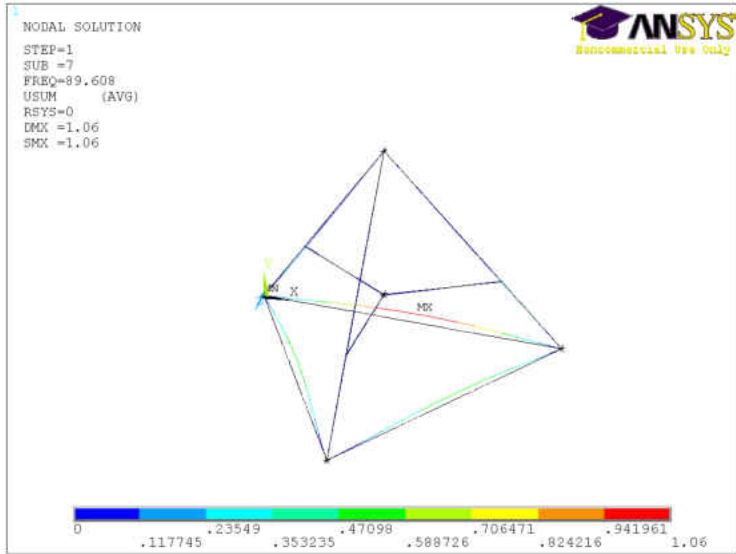
Figure 4-30 Mode 5 @ 89.6 Hz
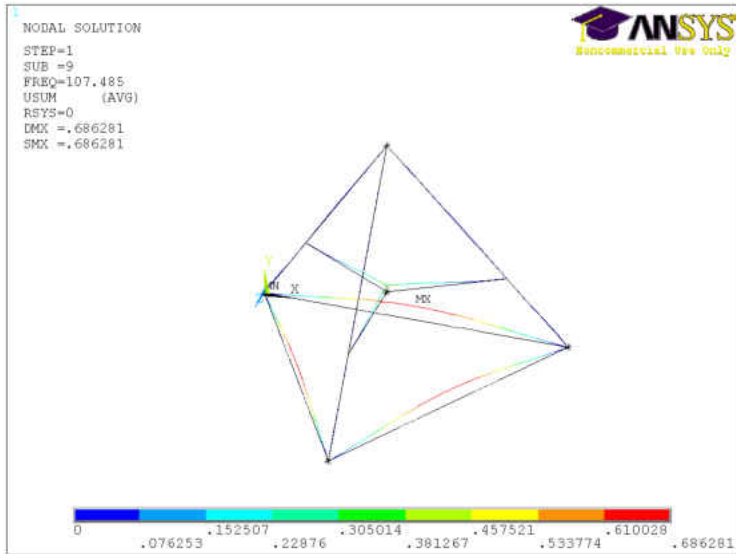
Figure 4-31 Mode 6 @ 107.5 Hz
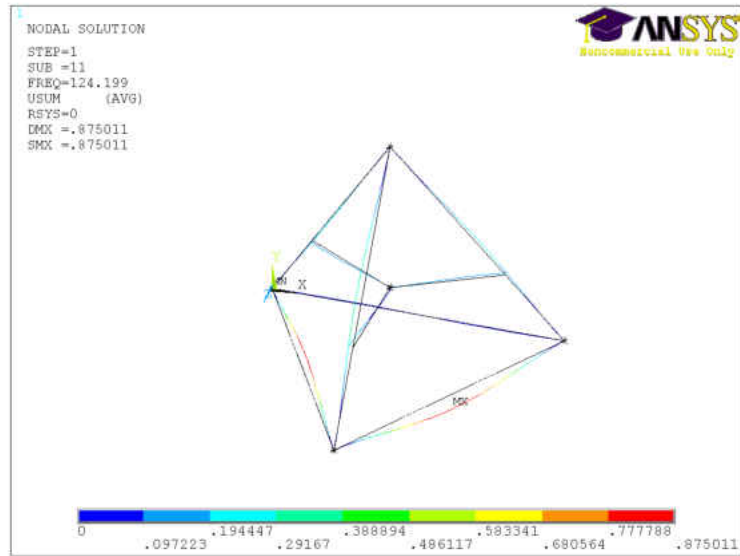
Figure 4-32 Mode 7 @ 124.2 Hz
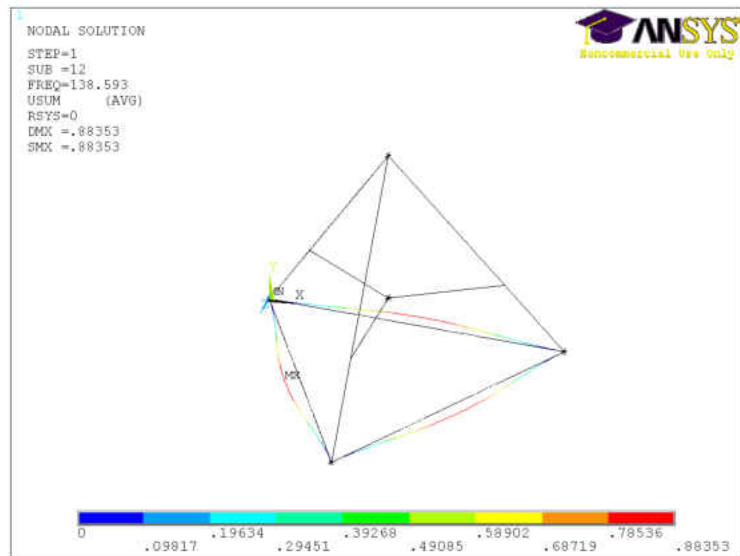
Figure 4-33 Mode 8 @ 138.6 Hz
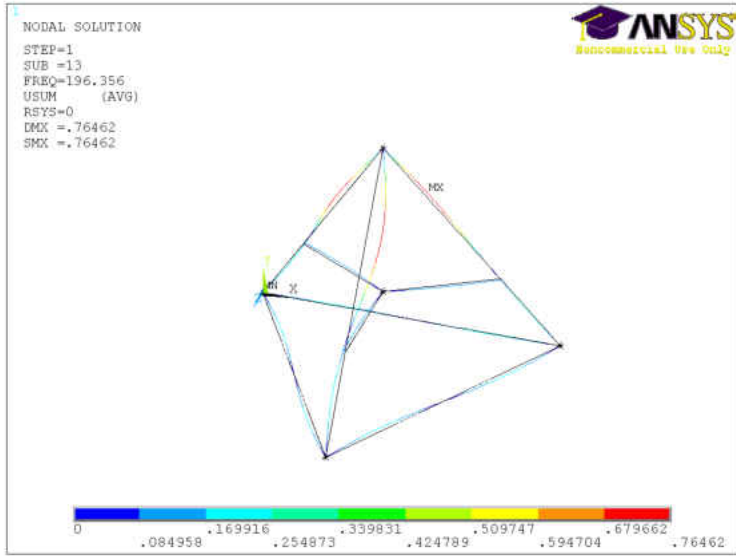
Figure 4-34 Mode 9 @ 196.4 Hz
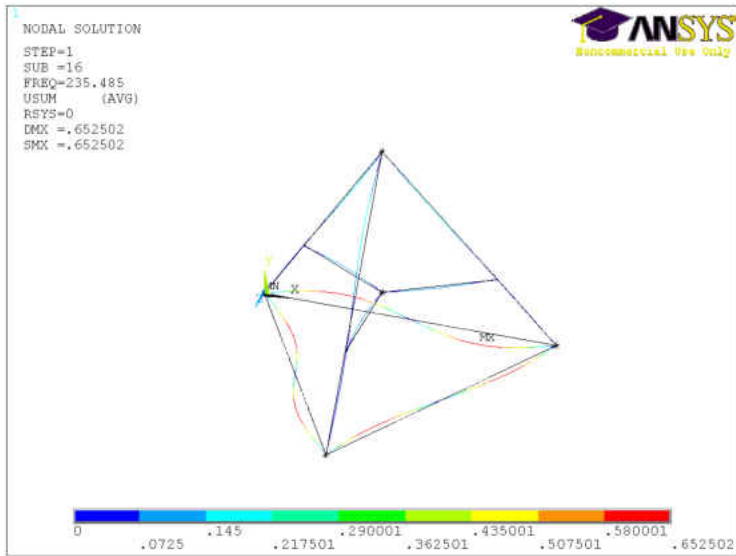
Figure 4-35 Mode 10 @ 235.5 Hz
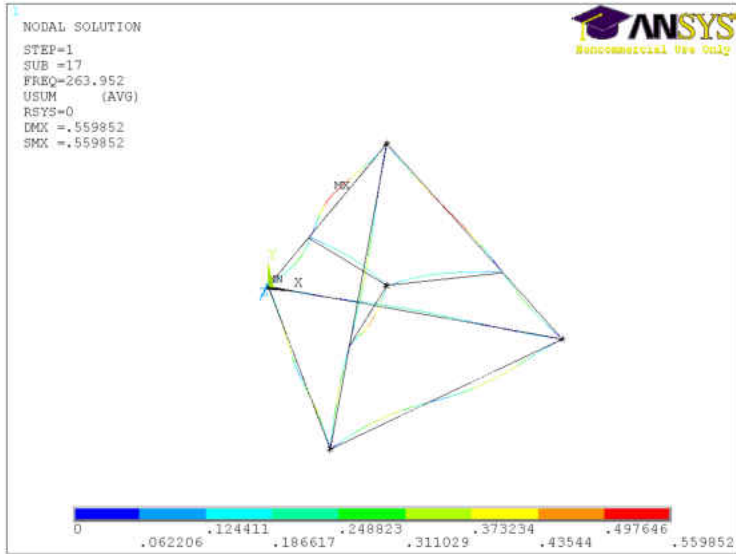
Figure 4-36 Mode 11 @ 264.0 Hz
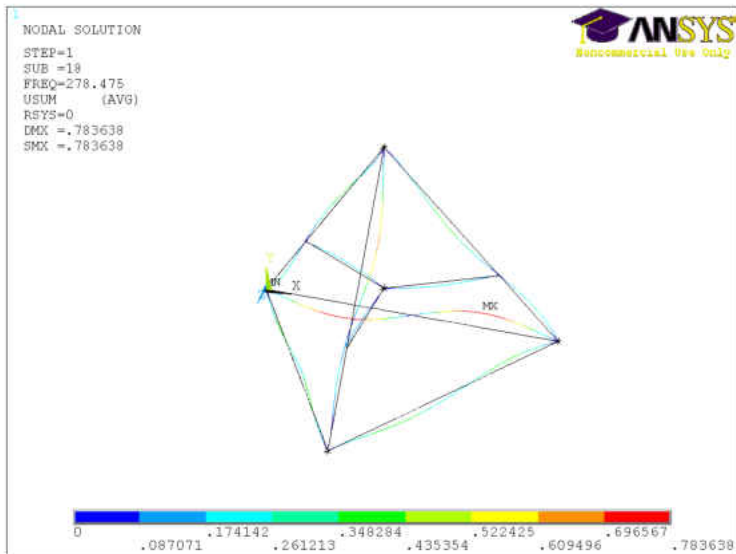
Figure 4-37 Mode 12 @ 278.5 Hz

Modes 4 and 6 both contain vertical displacement of the spindle holder. They both also have a large amount of energy in the lower beams. For Mode 4, the lower beams displace downward when the spindle moves upward. This mode is similar to Mode 5 of the Tetraform with the brackets and spindle. When removing the lower brackets, more of the energy is transferred to the lower portion of the Tetraform for this mode. For Mode 5, the lower beams and the spindle both displace in the same vertical direction. This mode is similar to Mode 1 of the Tetraform with the brackets and spindle. Removing the brackets for this mode creates more modal energy at the spindle location.

4.3   **Modal Analysis in Matlab**

Using the model that was created in Chapter 3 in Matlab, the natural frequencies, ω_n, can be calculated and checked with the ANSYS results. The structural equation of motion can be put into the form of (4.1). $[I]$ is an identity matrix and $\{\varphi\}$ is the eigenvector. $([K] - \omega_n^2 [I][M])$ is referred to as the dynamic stiffness matrix.

$$([K] - \omega_n^2 [I][M])\{\varphi\} = \{F\} \tag{4.1}$$

Taking the determinant of the dynamic stiffness matrix and setting it equal to zero yields a polynomial of ω_n^2 which are the eigenvalues of the system. The eigenvectors of the system are the relative nodal displacement vectors for their corresponding natural frequencies, or the mode shapes. The mode shapes will not be plotted in Matlab. However, they will be needed for converting the model to modal coordinates in the next chapter.

From the results of the Matlab code, the output results are a vector of eigenvalues and a matrix of the eigenvectors. These are represented by the variables D and V in the code. The eigenvalues are resorted in ascending order and the eigenvectors then needed to be rearranged to match their respective eigenvalues. The first 12 natural frequencies from the Matlab model are compared to the ANSYS results in Table 4-2. These values correspond well, validating the comparison of the Matlab dynamic results, in the next chapter, with the mode shapes plotted by ANSYS.

Table 4-2 Full Scale Tetraform Natural Frequencies without Spindle

Mode	1st	2nd	3rd	4th	5th	6th	7th	8th	9th	10th	11th	12th
Matlab (Hz)	41.7	52.1	64.6	65.1	98.5	103.5	114.3	144.0	203.6	208.5	242.3	293.9
ANSYS (Hz)	41.0	51.3	63.4	64.0	95.7	101.6	112.1	140.6	200.2	204.4	235.5	279.5

5   CHAPTER 5 – DYNAMIC ANALYSIS

5.1   <u>Introduction</u>

Dynamic analysis of the Tetraform is important to realize how different points on the structure respond to force inputs at different areas. FRFs were plotted to show the dynamic response between these points.   They consist of a magnitude response and a phase response. The magnitude plot shows the amplitude of the output vs. the frequency of the input where the amplitude is in decibels (dB) and the frequency is on the log scale in either radians/s or Hz. The phase plot shows the phase shift between the input force and the output response plotted vs. frequency on the log scale. These plots are also referred to as Bode plots. When carried out experimentally, the input force must be measured in order to compute the relationship between the input amplitude and phase to that of the output amplitude and phase.

The force inputs of interest are disturbance forces, machining forces, and actuator forces. Therefore, the FRFs were setup to display responses to these inputs. The relationship between responses of the spindle holder from machining forces were plotted to show which modes are easily triggered by machining. Similarly, the relationship between input disturbance forces at various points throughout the structure to the response of the spindle is important to show how easily the different critical modes can be triggered by external disturbances. These FRFs are also needed to determine the placement of the actuator to have the highest influence over the critical modes. Location of the actuators can be fine tuned by this method to find optimal placement for the vibration controller. Since the sensors and actuators are collocated, this location also allows

the sensor to receive the strongest response from the critical modes. It is also desirable for the sensor to have little response from non-critical modes.

Dynamic responses were conducted both experimentally and by simulation. Experimentally, the FRFs were obtained using the impact hammer method. This method uses an impact hammer to apply a measured impulse input while an accelerometer measures the dynamic response at the output point. Similar responses were also plotted by simulation to compare and validate the mathematical model. The simulation model was then used for structural analysis and design purposes due to the ease at which the inputs and outputs may be changed in simulation.

5.2 <u>Impact Hammer Method</u>

Experimental FRFs are most often obtained by one of two methods. The first method uses a force input of varying frequency to excite the structure while measuring the dynamic response with an accelerometer. A common device used to apply the force input for this method is a shaker. A shaker either mounts the test object on top of it or applies the input force to a point by way of an armature. Forcing frequency is then varied to measure the amplitude and phase of the response for a range of frequencies.

The alternative method is that of the impact hammer method. A hammer is used to apply an input that acts as an impulse. An impulse is a force input of constant amplitude and infinitely small duration. Ideally, this input triggers the entire frequency. In actuality, the hammer force input cannot be of infinitely small duration. Interchangeable hammer tips may be used to obtain

responses from different ranges of the frequency spectrum. The harder tips create shorter time of impacts and are used to trigger higher frequencies.

The impact hammer contains a load cell to measure the input force while the dynamic response is measured from accelerometers. The input and output signals are then compared to give the FRF. A 086C03 impact hammer from PCB, shown in Figure 5-1, was used as the impact force transducer. Two single-axis PCB 352C65 and one tri-axis PCB 356A32 were used for the accelerometers.

Figure 5-1 PCB Impact Hammer

It should also be noted that all FRFs were conducted while the spindle motor and bearing were mounted in the spindle holder. It was found that the different modes were not clearly defined without this added mass of the spindle motor and bearing due to the high dynamic stiffness in the closed loops of the structure along with the localized damping of the brackets and

joints. The addition of the mass and inertia of the spindle motor and bearing will also more accurately represent the Tetraform under machining conditions.

Multiple impact hammer responses were conducted on the full scale Tetraform. These were used to verify the FEA simulation models and to obtain damping values. Damping must be added to the FEA models in order to accurately simulate any type of forced response. The comparison of these results with the FEA model results are shown at the end of the chapter.

5.3   Matlab Simulation

The FEA model must be converted to a form that will give the displacement response to a force input. Therefore, the model must be reduced in size, damping must be added, and then must be converted over to state space. The FEA model that was created in Matlab, (5.1), must be converted into a form that will give the displacement response to force inputs. Therefore, it was required that the model be reduced in size, damping to be added, and the model to be converted to state space.

$$[M]\{\ddot{r}\} + [K]\{r\} = \{f\} \qquad\qquad (5.1)$$

This model contains 101 nodes with six degrees of freedom at each node. The size of this model creates much difficulty in computation during simulation. By using the method of decoupling the model into modal coordinates, we can reduce the size of the model significantly. This is done by using the eigenvectors that were solved from the model described in (5.1) to manipulate the mass and stiffness matrices into decoupled equations of motion in modal

coordinates. An eigenvector matrix $[\Phi]$ was constructed from the eigenvectors φ_i where $i = 1:n$ and n is the number of degrees of freedom. These were sorted in ascending order where φ_1 is the eigenvector of the first mode.

$$[\Phi] = [\varphi_1 \quad \varphi_2 \quad \cdots \cdots \quad \varphi_n] \tag{5.2}$$

Using this modal matrix, the dynamic equation is converted from structural coordinates, $\{r\}$, to modal coordinates, $\{q\}$. Equation (5.3) shows the conversion between the two coordinates. By plugging this into (5.1) and multiplying through by $[\Phi]^T$ results in (5.4).

$$\{r\} = [\Phi]\{q\} \tag{5.3}$$

$$[\Phi]^T[M][\Phi]\{\ddot{q}\} + [\Phi]^T[K][\Phi]\{q\} = [\Phi]^T\{f\} \tag{5.4}$$

Due to orthogonality of the eigenvectors, the mass and stiffness matrices are diagonalized into the modal mass and stiffness matrices shown in Eqs. (5.5) and (5.6). Here, m_i and k_i are the modal mass and stiffness values for the ith mode.

$$[\Phi]^T[M][\Phi] = [M'] = \begin{bmatrix} m_1 & 0 & \cdots & \cdots & 0 \\ 0 & m_2 & 0 & \cdots & 0 \\ \vdots & 0 & m_3 & 0 & 0 \\ \vdots & \vdots & 0 & \cdots & 0 \\ 0 & 0 & \cdots & 0 & m_n \end{bmatrix} \tag{5.5}$$

$$[\Phi]^T[K][\Phi] = [K'] = \begin{bmatrix} k_1 & 0 & \cdots & \cdots & 0 \\ 0 & k_2 & 0 & \cdots & 0 \\ \vdots & 0 & k_3 & 0 & 0 \\ \vdots & \vdots & 0 & \cdots & 0 \\ 0 & 0 & \cdots & 0 & k_n \end{bmatrix} \tag{5.6}$$

Equation (5.7) is the new dynamic equation in modal coordinates. This shows the response is the superposition of n uncoupled modal equations. The number of eigenvectors, n, may then be limited to the highest mode of interest. With 101 nodes and six degrees of freedom at each, there are 606 eigenvectors before removing nine through boundary conditions. As a majority of the higher modes are dampened out and nonexistent in reality, the number of included modes can be greatly reduced.

$$[M']\{\ddot{q}\} + [K']\{q\} = \{f'\} \tag{5.7}$$

Once the model in modal coordinates is reduced, damping may be included. The damping matrix is determined by Rayleigh's damping coefficients, α and β, and is given in (5.8). These coefficients are determined from experimental results. For this simulation, damping will be given the values $\alpha = 2$ and $\beta = 3e - 5$. The equation of motion with damping is now (5.9).

$$[D] = \alpha[M'] + \beta[K'] \tag{5.8}$$

$$[M']\{\ddot{q}\} + [D]\{\dot{q}\} + [K']\{q\} = \{f'\} \tag{5.9}$$

Converting the equation of motion to state space form gives an output vector of displacements, $\{y\}$, to an input vector, $\{u\}$. The size of the input and output vectors depends on the number of inputs and outputs of the system. For frequency responses, only one of each is required, making these terms scalar. The second order differential equations from (5.9) will be separated into first order equations by defining the state vector, $\{\xi\}$, in (5.10).

$$\{\xi\} = \begin{Bmatrix} \{q\} \\ \{\dot{q}\} \end{Bmatrix} \qquad (5.10)$$

Redefining the system in terms of the state vector gives Eqs. (5.11) through (5.14) where $\{f\}$ is the force input vector and $[C]$ is the output matrix. These are defined based on the input and output locations on the Tetraform. For these simulations, the feed through matrix, $[D]$, is set to zero. The sensor responses used the piezoelectric sensor equations that are defined in Chapter 6.

$$\{\dot{\xi}\} = [A]\{\xi\} + [B]\{u\} \qquad (5.11)$$

$$\{y\} = [C][\Phi]\{\xi\} + [D]\{u\} \qquad (5.12)$$

$$[A] = \begin{bmatrix} 0 & I \\ -[M']^{-1}[K'] & -[M']^{-1}[D] \end{bmatrix} \qquad (5.13)$$

$$[B] = \begin{bmatrix} 0 \\ -[M']^{-1}[\Phi]^T\{f\} \end{bmatrix} \qquad (5.14)$$

5.4   Interpretation of Results

Since the impact hammer method used accelerometers for the response, the FRFs reflect the relationship between acceleration outputs to a force inputs. The previously made FEA model was set up to output displacement. Just for the purpose of comparison to the experimental plots, the state space model was converted to acceleration output. This was done by multiplying the output by the transfer function s^2. All the FRFs that were not compared to experimental results were kept as position responses.
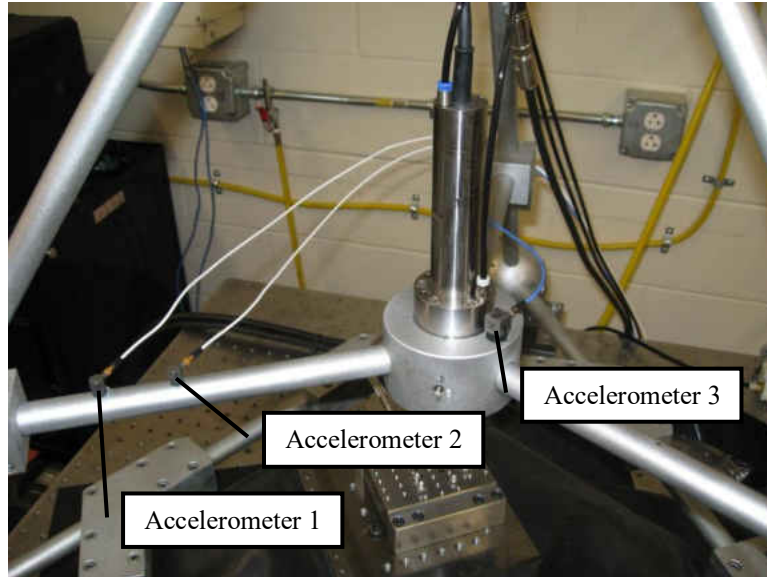
Figure 5-2 Accelerometer Locations

Three impact hammer responses were attained for comparison with the FEA model. The impacts were applied in the vertical direction on the spindle holder. Three accelerometer locations then measured the response. The location of these accelerometers is shown in Figure 5-2. Figures 5-3 through 5-5 show the comparison between the theoretical and experimental FRFs. The experimental phase plot has been shifted positive to become comparable to the theoretical phase plot.
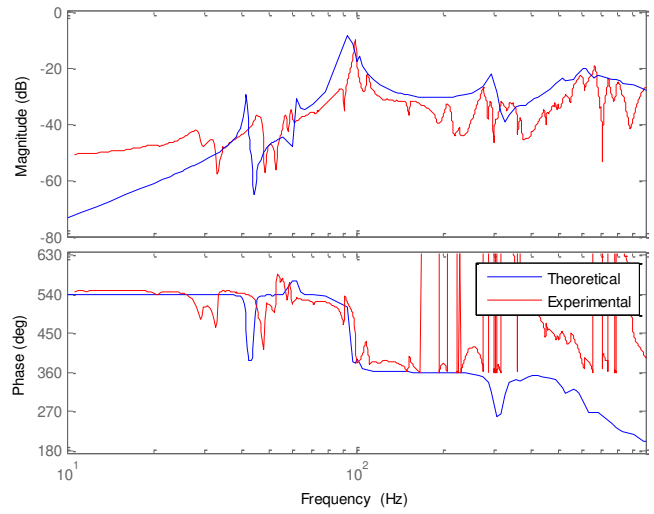
Figure 5-3 Accelerometer 1 Response to Vertical Input at Spindle
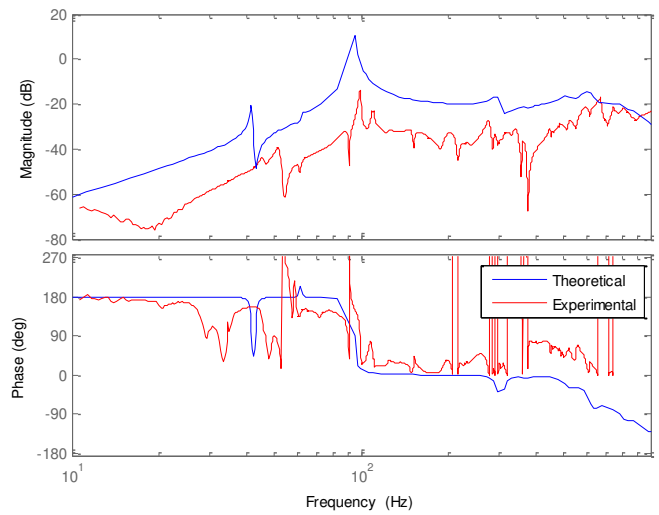
Figure 5-4 Accelerometer 2 Response to Vertical Input at Spindle
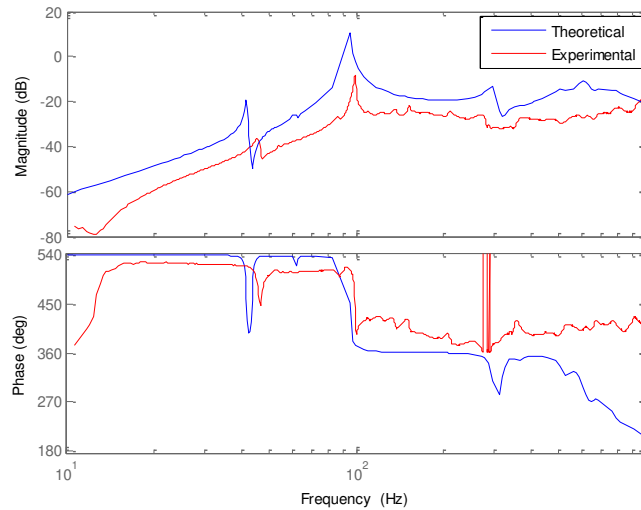
Figure 5-5 Accelerometer 3 Response to Vertical Input at Spindle

The theoretical and experimental results correspond very well. For the experimental response, it can be seen that some of the peaks are separated into multiple frequencies. Ideally, symmetric modes have the exact same frequency and would display one peak. In reality, structures almost never display perfectly symmetric modes. Because of the high dynamic stiffness of the closed loops of the Tetraform and localized damping of the brackets and joints, the non-symmetry of the modes is exploited. Also, some of the theoretical peaks are shifted in the frequency domain. Assumptions made while creating the model could have under or over estimated the mass and stiffness of certain areas of the Tetraform. These differences will change the peaks as an increase in stiffness or mass will shift the natural frequency positive or negative respectively. Overall, the FRF curves support the use of the FEA model for dynamic analysis and vibration control simulations.

The rest of the figures in this chapter display displacement responses as opposed to acceleration responses. The following FRFs are used to test modal displacements of the spindle from machining forces, disturbance forces, and actuator forces. It is desirable to have minimum modal displacements from the machining and disturbance forces while having maximum modal displacements from the actuators. Therefore, FRFs were set up to display which modes were triggered by force inputs at locations representing machining forces and disturbance forces. Then, different actuator locations were tested to verify their controllability over those modes.

The responses in Figures 5-6 and 5-7 show the response of the spindle to force inputs at the spindle. These show the dynamic stiffness of the spindle to machining forces. The displacement outputs were setup to correspond to force inputs in the same direction. In other words, the x axis response is to a force input in the x direction. If a mode has significant displacement at the spindle point then it will be easily triggered by a force in that displacement direction. For the model created, the z axis is in the vertical direction while the x and y axis lie on the horizontal plane. For reference, the Tetraform natural frequencies with the spindle added are displayed in Table 5-1.

Table 5-1 Tetraform Natural Frequencies with Spindle Added

Mode	1st	2nd	3rd	4th	5th	6th	7th	8th	9th	10th	11th	12th	13th
(Hz)	41.6	51.5	61.9	65.1	94.8	98.3	101.5	143.9	203.6	207.5	242.2	274.6	297.2
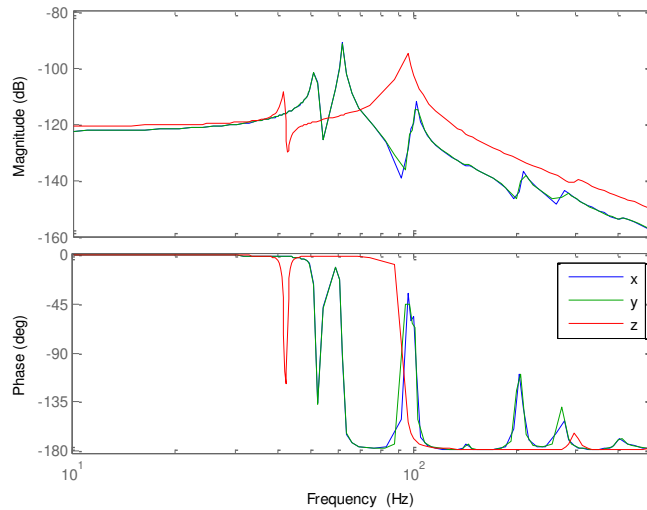
Figure 5-6 Translational Force Responses of Spindle

There are significant peaks at about 41, 51, 61, 98 and 101 Hz. Comparing the responses with the made shapes in the previous chapter helps to understand the magnitudes of the spindle displacements. The peaks at 41 and 94 Hz affect the spindle in the vertical direction and correspond to the 1st and 5th mode shapes. Neither of these modes include horizontal displacements. The 1st mode acts as a loop between the lower and inner arms. Most of its energy is contained in the lower potion of the structure but still creates some vertical displacement to the spindle. The 5th mode is the vertical motion of the spindle mass attached to three beams. Most of its modal energy is contained in the inner portion of the Tetraform and creates large vertical displacement of the spindle. The peaks at 51, 61, and 101 Hz correspond to the 2nd, 3rd and 6th modes. These only affect the horizontal displacements of the spindle. The 2nd and 3rd are bending modes of the entire Tetraform. The 2nd contains most of its energy in the

lower portion of the Tetraform while the 3rd contains most of its energy above the brackets giving it the larger spindle displacement.

In addition to the translational responses of the spindle, rotational responses were also studied. Three torques were applied to the spindle to obtain responses to their respective degrees of freedom. The magnitude of the rotational responses cannot be directly compared to the magnitude of the translational responses as rotational displacements and forces have different units than rotational displacements and forces. The rotational plots are still important to understand which modes can be triggered by machining forces.
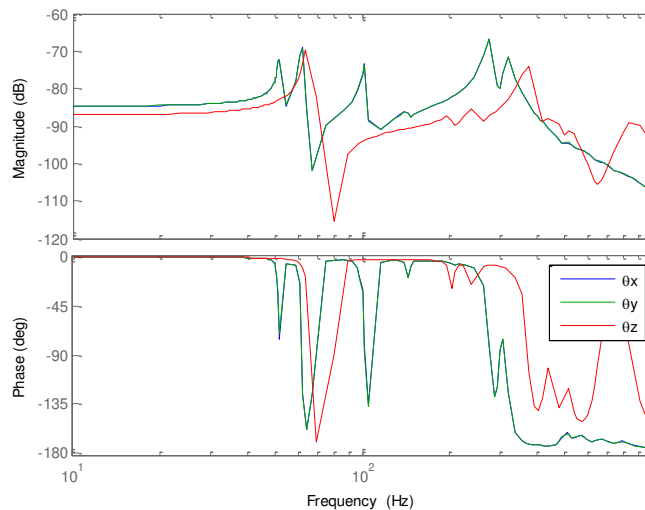

Figure 5-7 Torque Responses of Spindle

This shows that some higher frequency modes contain more energy than the lower modes for rotation of the spindle. This is a partial indication of there being little rotation of the spindle involved with the lower modes. These higher modes do show up in the horizontal response of

Figure 5-6 but contain much less modal energy than the lower modes for the spindle location. However, these higher modes are still of importance.

The translational responses of the spindle to applied torques at the spindle were plotted in Figures 5-8 through 5-10 to show the coupling between the translational and the rotational degrees of freedom. For these plots, the three torque inputs were applied at the spindle while the output is a single degree of freedom at the spindle. This could have been done inversely by applying one torque and measuring the output in different degrees of freedom for the spindle. These FRFs would be interchangeable. This comes from Maxwell's Theorem of Reciprocity which is applicable to linear structures. When looking at the force-displacement relationship between two points on the structure, the displacement of point 1 from a unit force on point 2 is equal to the displacement of point 2 from a unit force on point 1. This means that the FRF will be equal in both directions between the two points. This property is true because of the symmetry of the mass and stiffness matrices for linear structures.
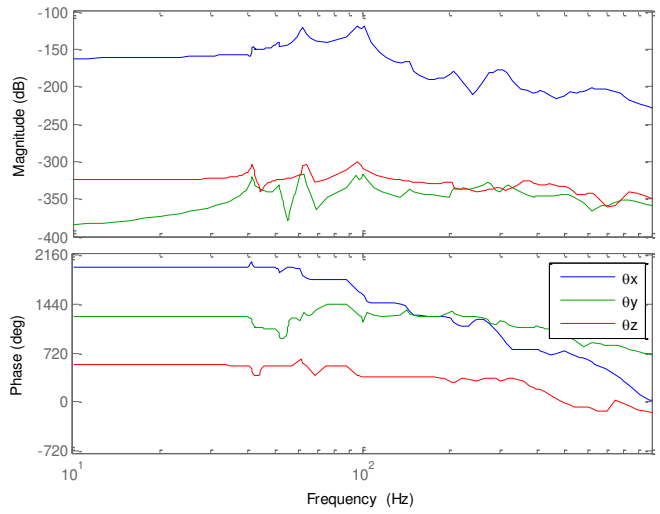
Figure 5-8 Z axis Spindle Response to Torque Inputs at Spindle
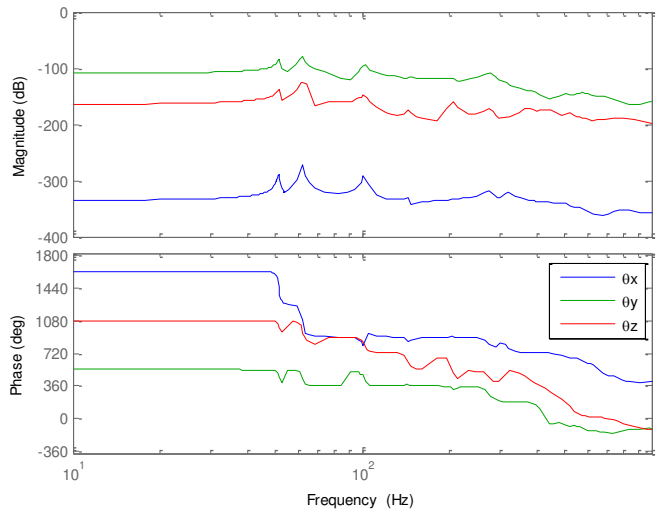
Figure 5-9 X Axis Spindle Response to Torque Inputs at Spindle
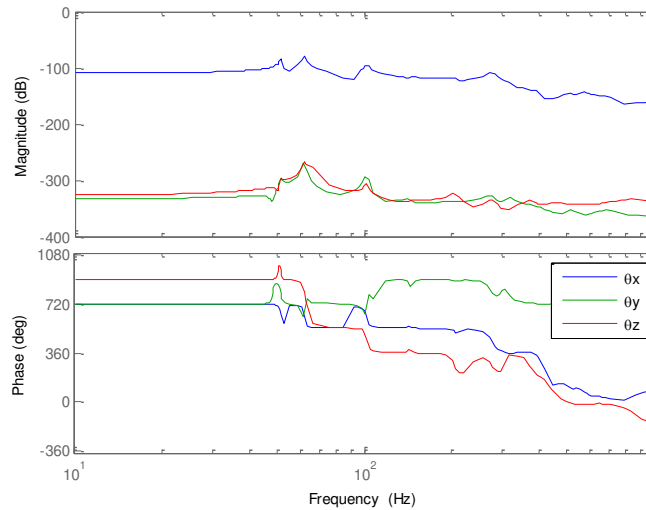
Figure 5-10 Y Axis Spindle Response to Torque Inputs at Spindle

From Figures 5-8 through 5-10 it is determined that there are three significant translational peaks that can be produced by spindle torques. These are the 2nd, 3rd, and 7th modes. The strongest responses come in the horizontal directions while the vertical displacement of the spindle shows less responsiveness to spindle torques. It should be noted again that the magnitudes of these plots are not directly comparable to the magnitudes of the translational force plots. For the machining process, the translational force (N) will be much higher than the torque (N/m).

Next, the affect of disturbance forces on the spindle location are tested. Inputs were applied perpendicular to the beam at three points and in the vertical direction to the top sphere. These locations are illustrated in Figure 5-11. Their spindle displacement responses were measured on the x, y, and z axis. The spindle responses for these disturbances are displayed in Figures 5-12 through 5-15.

71
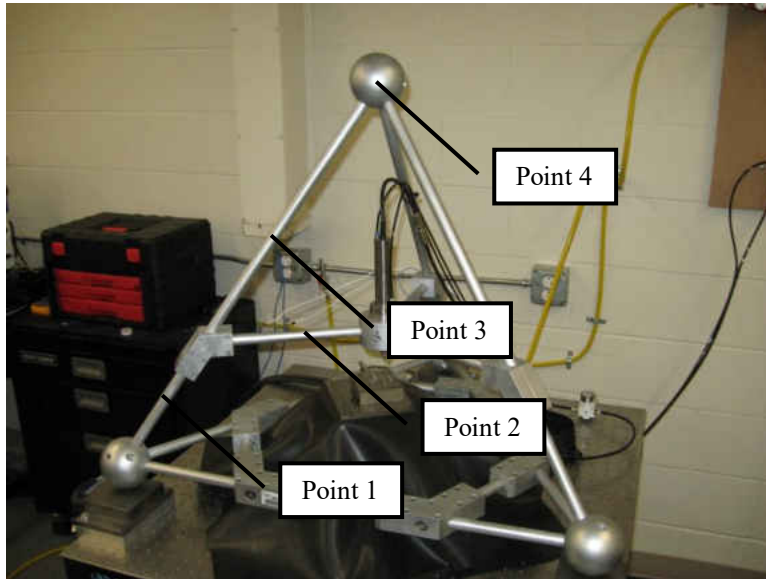
Figure 5-11 Disturbance Locations
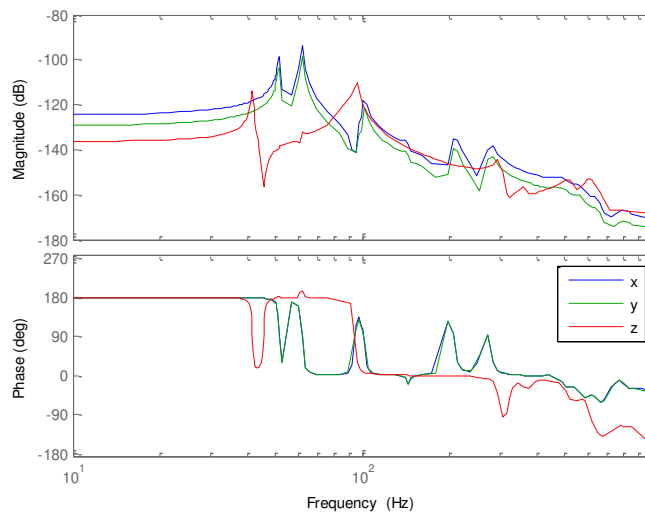
Figure 5-12 Response of Spindle to Perpendicular Force at Point 1
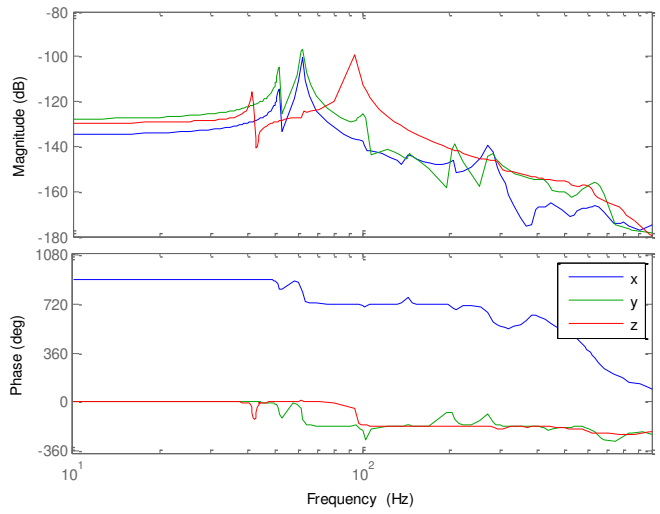
Figure 5-13 Response of Spindle to Perpendicular Force at Point 2
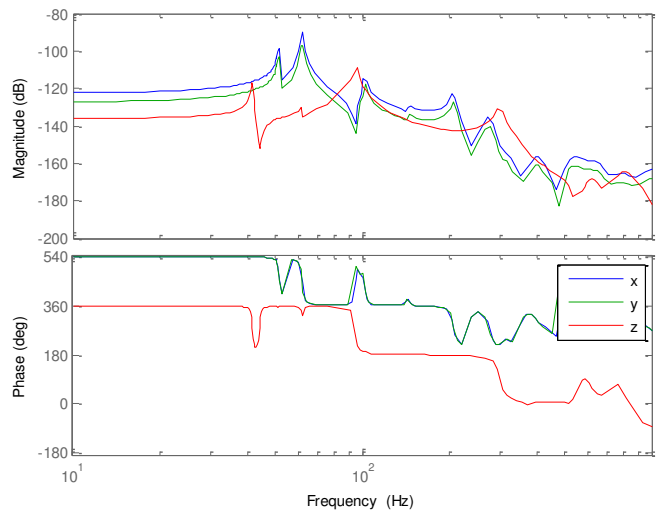
Figure 5-14 Response of Spindle to Perpendicular Force at Point 3
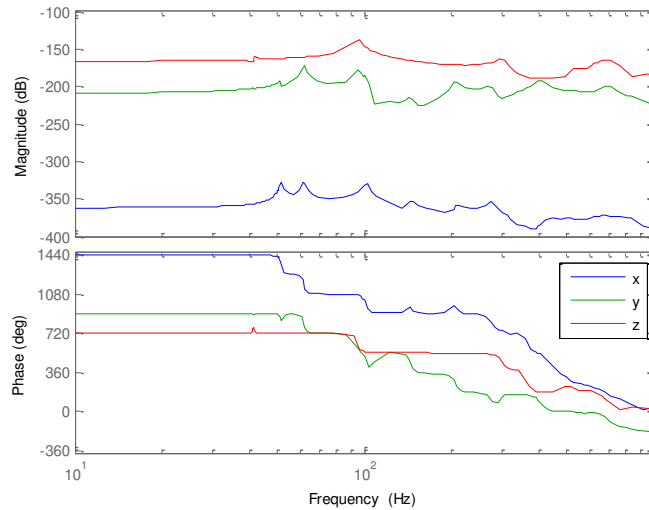
Figure 5-15 Response of Spindle to Vertical Force at Point 4

The 2nd and 3rd modes can easily be triggered by disturbances to most areas of the structure. The 6th mode, which is one of the highest energy modes for the spindle, is mostly triggered by disturbances to the inner arms. While inputs to the lower portion of the structure have more of an affect on modes with horizontal spindle displacements, the 1st mode can also be triggered here. It is also seen that Point 4 has the least affect on most modes.

The effects from actuator forces on the spindle location were also tested. The goal was to mount the actuator in a location that would create the highest modal displacement at the spindle point. This ensures the most efficient control over the critical modes. The actuators contract and expand in the longitudinal direction creating a surface strain on the beam. This applies both an axial force and a bending moment on the beam. For these FRFs, the input was set up as a unit force between two nodes along with its corresponding bending moments. The output was set up

as the displacement of the spindle. The three actuator locations being tested are shown in Figure

5-16. The comparison of these three locations is shown in Figures 5-17 to 5-19.
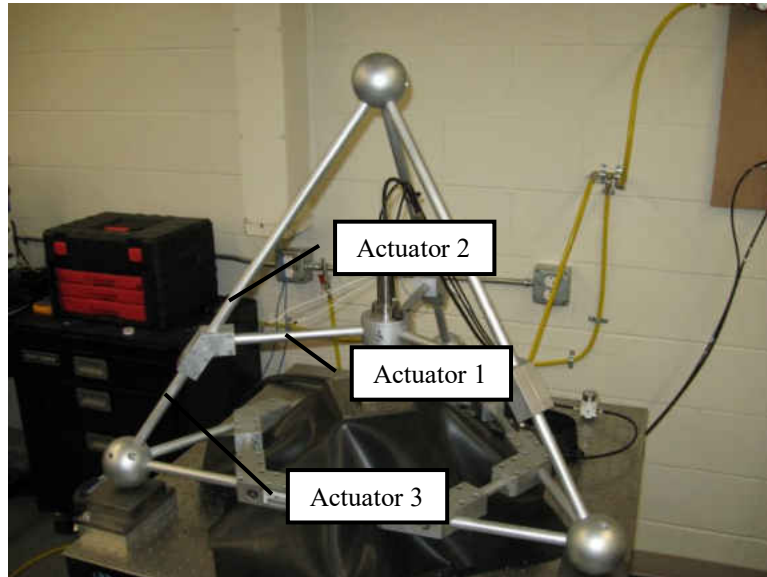
Figure 5-16 Actuator Test Locations
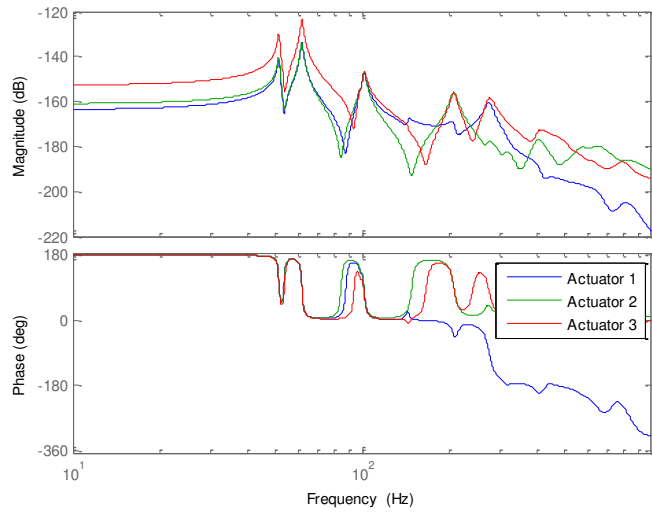
Figure 5-17 Spindle X-Axis Response to Actuators
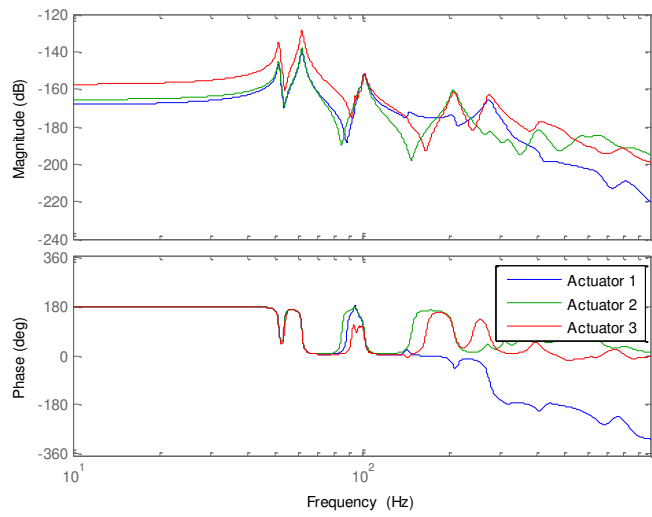
Figure 5-18 Spindle Y-Axis Response to Actuators
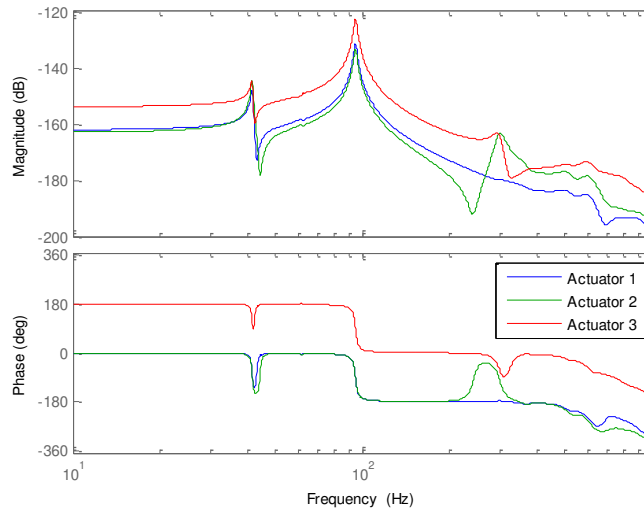
Figure 5-19 Spindle Z-Axis Response to Actuators

Figures 5-18 through 5-19 show that location 3 has more influence than the other two locations for nearly every mode. Location 3 shows the ability to control these modes more effectively than the other two locations. Also, since the sensors are collocated, location 3 is where the sensor would be most sensitive to the critical modes. However, it will be seen in the next chapter that there is a negative effect from using location 3. The higher DC gain from this location can decrease the static stiffness of the Tetraform after the active vibration controller is applied.

6   CHAPTER 6 – ACTIVE VIBRATION CONTROL

6.1   <u>Piezoelectricity</u>

Piezoelectricity is the coupling affect of mechanical and electrical properties. When a piezoelectric material is subjected to a mechanical stress, a resulting electrical charge develops towards the surface of the material. The inverse affect is also present in the material. When a voltage is applied across the material, a mechanical strain is produced. This piezoelectric phenomenon is a property in natural crystalline materials such as quartz and Rochelle Salt. However, due to a small coupling affect, these materials are insufficient for use in most engineering applications. Ceramics have been developed that demonstrate high piezoelectric coupling properties. These include Lead Zirconate Titanate ceramics (PZT). PZT is one the most commonly used materials for piezoelectric applications. Its strong coupling properties make it ideal for vibration control applications.

The coupled elastic and electric equations for piezoelectric material stressed in the longitudinal direction, axis 1, and polarized in the transverse direction, axis 3, are given in (6.1) which is an IEEE standard [12]. Here, ϵ is the strain, D is the electrical displacement (charge/area in the transverse direction), $\bar{E}$ is the electrical field (voltage/length in the transverse direction), S_{p11} is the elastic compliance, ε_{33}^{T} is the dielectric constant, and d_{31} is the piezoelectric strain constant. The strain constant relates an input voltage on axis 3 to an output strain on axis 1 per unit length of width. This is used to derive the actuator equation. Another useful property is the piezoelectric stress constant, g_{31}, which is used to relate an applied stress

in axis 1 to the resulting voltage in axis 3. This is used to derive the sensor equation. These constants are readily available from the manufacturer.

$$\begin{Bmatrix} \epsilon \\ D \end{Bmatrix} = \begin{bmatrix} S_{p11} & d_{31} \\ d_{31} & \varepsilon_{33}^T \end{bmatrix} \begin{Bmatrix} \sigma \\ \bar{E} \end{Bmatrix} \qquad (6.1)$$

6.2   Active Damping Modeling

Mide Technology Corporation was chosen as the supplier for the piezoelectric transducers. They produce flexible transducers that conform to curved surfaces. This was one of the primary concerns when selecting the transducer for this application. The Tetraform beams are tubular with an outside diameter of ¾". PZT is a brittle material that is generally used as an actuator-sensor where it can be bonded to a flat surface. The Mide pa16n transducers consist of strips of PZT in the longitudinal direction of the beam. This allows the patch to be bent to the form of the curved surface without putting any stress on the PZT strips. That makes them ideal for this curved surface with a small radius of curvature.

Table 6-1 Piezoelectric Material Properties

ρ (kg/m^3)	ε_{33}^T	d_{31} (m/V)	g_{31} (V-m/N)	E_{11} (N/m^2)
7700	800	-179E-12	-11.0E-3	6.9

The material properties for the pa16n transducer are shown in Table 6-1 and have the dimensions of 5.21 x 3.02 x 0.003 cm. The performance curves for different voltages are shown in Figure 6-1. The patch has an operating range of +/- 120V.
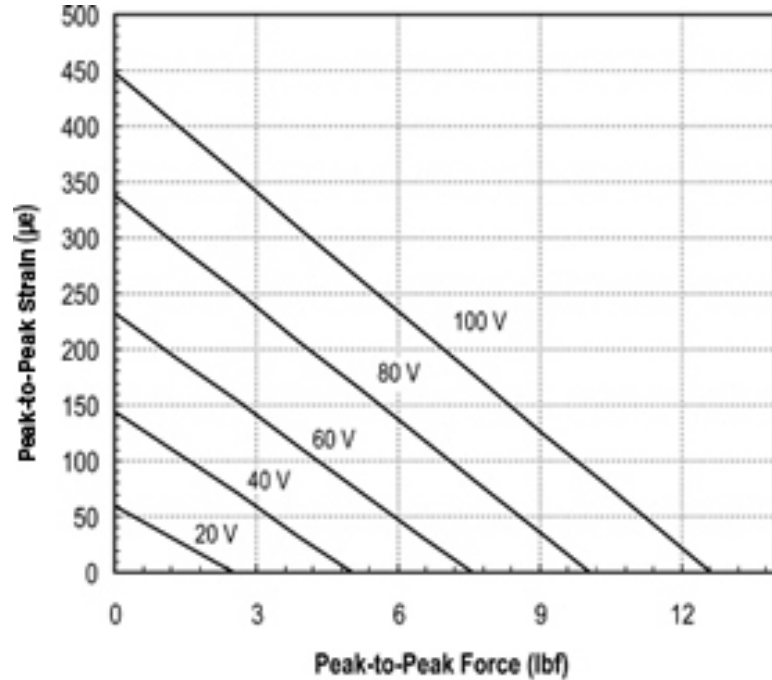
Figure 6-1 Mide pa16n Transducer Performance [20]

The FEA model that was created in Matlab, (6.2), will now be put into a form that can be controlled in an active vibration simulation. The stiffness and mass of the piezoelectric transducers must be included in the structural matrices. The sensor and actuator equations must then be developed for the input and output matrices of the state space model.

$$[M']\{\ddot{q}\} + [D]\{\dot{q}\} + [K']\{q\} = \{f'\} \tag{6.2}$$

The sensors and actuators patches were modeled as beams to include in the structural mass and stiffness matrices. These were modeled in a similar manner as the frame beams but with the moments of inertia calculated about the tubular beam's axes. The smart structure finite element model was converted to state space, therefore the actuator and sensor equations needed to be developed in input and output vector format [6, 7]. Using (6.1), the actuator force vector $\{f_a\}$ is shown in (6.3) and (6.4) where $u(t)$ is the input voltage, E_p is the piezoelectric Young's Modulus, r is the radius of the axial force created by the patch, and b is the width of the contact area between the patch and beam. Equation (6.4) shows that this vector represents the actuator axial force, F_{ax}, and the actuator bending moment, M_{ay}. These forces are applied at the end nodes of the piezoelectric elements. The sensor voltage vector, ϕ, is given in (6.5) where t is the patch thickness. The stress in the sensor equation is created from both bending and axial forces and is evaluated at the end nodes of the piezoelectric elements.

$$f_a = u(t)E_p d_{31} b\{-1 \quad r \quad 1 \quad -r\}^T \tag{6.3}$$

$$f_a = \{-F_{ax} \quad M_{ay} \quad F_{ax} \quad -M_{ay}\}^T \tag{6.4}$$

$$\phi = -\frac{t}{L_e} g_{31} E_p \left([r\theta_y - u]_{nodej}^{node\ i}\right) \tag{6.5}$$

The input matrix, $[B]$, is given in (6.6) where $[f_a]$ is the matrix made up of the actuator input vectors. The output matrix, $[C]$, is given in (6.7) where $[\phi]$ is a matrix made up of the sensor output vectors.

$$[B] = \begin{bmatrix} 0 \\ -[M]^{-1}[\Phi]^T[f_a] \end{bmatrix} \tag{6.6}$$

$$[C] = [[\phi] \quad 0] \tag{6.7}$$

6.3   Controller

A positive position feedback controller will be used in targeting the critical modes. One common task in vibration control is overcoming spillover, which is the affect of out of bandwidth modes on the controller. This can destabilize the controller [9]. The PPF controller was chosen for its ability to minimize the effect of the out of bandwidth modes [8]. The dynamics of the controller resemble that of a mass-spring-damper system being applied to the structure, which the response naturally rolls off after a certain frequency, making it invulnerable to higher frequencies. Shown in Figure 6-2 is the bode plot of a PPF filter.
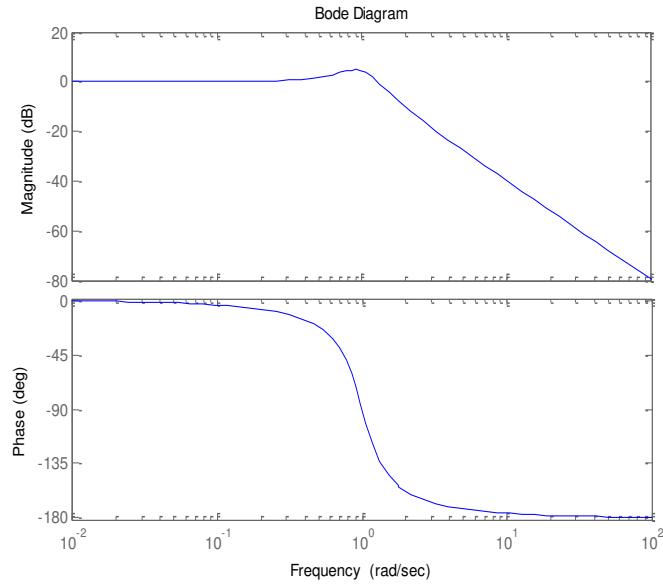
Figure 6-2 Bode Plot of PPF Filter

Positive position feedback is a second order compensator which is forced by the structural displacement. The equations that describe the PPF compensator are given in Eqs. (6.8) through (6.11) [10, 11]. Equation (6.8) describes the dynamics of the structure and (6.9) describes the dynamics of the controller input.

$$[M]\{\ddot{\xi}\} + [C]\{\dot{\xi}\} + [K]\{\xi\} = \left[B_f\right]\{u\} \tag{6.8}$$

$$\{\ddot{\eta}\} + 2\zeta_c\omega_c\{\dot{\eta}\} + \omega_c^2\{\eta\} = \omega_c^2\left[C_f\right]^T\{\xi\} \tag{6.9}$$

$$\{u\} = g\{\eta\} \tag{6.10}$$

$$\phi = \left[C_f\right]^T\{\xi\} \tag{6.11}$$

83

Here, $\{\xi\}$ is the modal coordinate state vector, $\{\eta\}$ is the controller coordinate vector, g is the controller gain, ω_c is the compensator frequency, and ζ_c is the compensator damping. $[B_f]$ is the input matrix for the control signal $\{u\}$. The control signal is a vector because there is a controller for each of the three collocated patch/sensor pairs. The control system then takes the form shown below in Fig. 6-3. The plant is represented with the state space model previously developed where the output $\{\xi\}$ is directly proportional to the surface strain of the beam. The damping constant and natural frequency for the controller are chosen to best target the critical modes. As ω_c is increased, so will the roll off frequency [10].

Figure 6-3 Positive Position Feedback Controller

6.4   Results

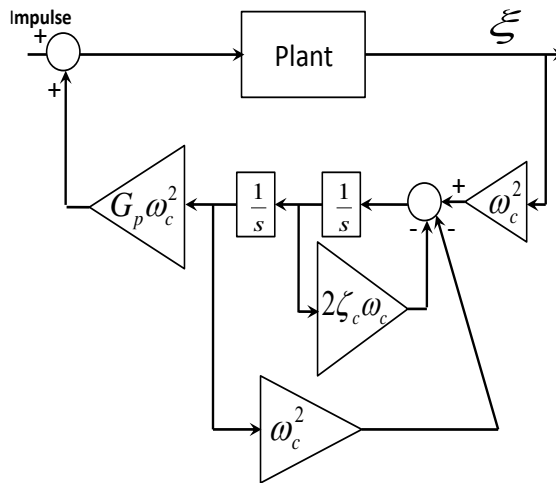The first test location for the actuator/sensor pairs will be location 1 described in the previous chapter. Each of the transducer pairs will be placed at this position on the three inner spindle arms. With the three pairs placed equal distance from the spindle on the inner beams, the frequency responses will also be equal. Therefore, the controller for each pair will contain the same constants. It was chosen to target the frequency at 94 Hz which is the dominant mode for the spindle z-direction.

Root locus was used for tuning of the controller. Root locus plots show how the closed loop poles move in the complex domain as a chosen constant is varied. It was found that with higher controller damping, ζ_c, a higher controller gain, g, was required to achieve desirable decibel reduction for the target frequency. However, when the controller damping is decreased too much, the controller poles tend to become more dominant, creating their own magnitude peaks. For this controller, ζ_c was chosen to be 0.4. The value of the controller natural frequency, ω_c, was chosen to maintain a -90 degree phase shift at the target frequency. For this controller, ω_c is placed at 97 Hz.

Figure 6-4 shows the root locus for varying the controller gain from 0 to 650. The largest movement is seen from the controller poles and the targeted structural poles. As the gain increases the targeted structural poles are driven to a location of higher damping. The controller poles tend toward the real axis and then move positive and negative on this axis. Increasing the gain beyond this point would push the controller pole into the right side of the imaginary axis, causing the controller to become unstable. The affect of the lower frequencies is also seen here.

85

Although not as much movement is created in these poles, there is damping added to some lower frequencies. It can also be seen that very little movement is seen from the higher frequency structural poles. This corresponds with the controller rolling off after the target frequency.
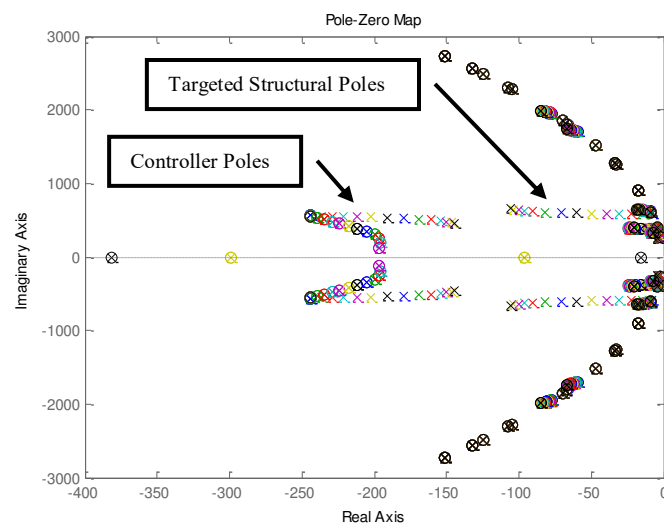
Figure 6-4 Root Locus Plot for Actuator Location 1

With the controller gain set at 650, the controlled structural responses are investigated. Figure 6-5 shows the vertical frequency response of the spindle to a vertical force at the spindle for both the uncontrolled and controlled Tetraform models. This shows significant decibel reduction for the target frequency at 94 Hz. This response also demonstrates that a PPF controller can also decrease the static stiffness of the structure as the DC gain is raised for the controlled response. The frequency plot also verifies that the -90 degree phase shift is maintained for the chosen controller frequency.
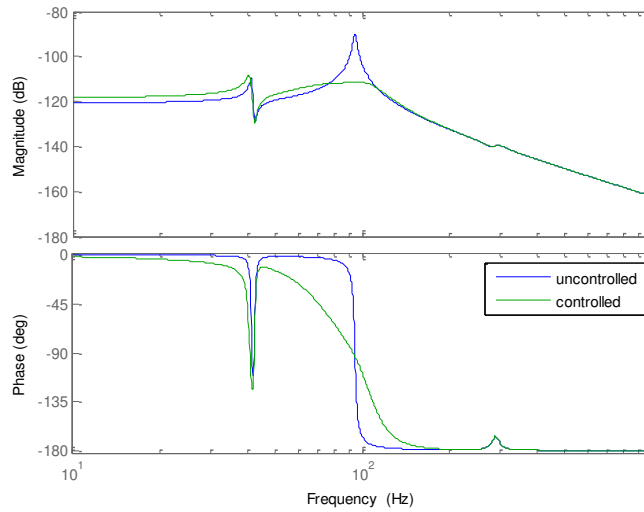
Figure 6-5 Vertical Spindle Frequency Response for Actuator Location 1

The affect of the controller on a vertical impulse response of the spindle is shown in Figure 6-6. This corresponds to the frequency response where the dominant frequency is all but eliminated. The lower frequency remains unchanged but has relatively little amplitude in the spindle response.
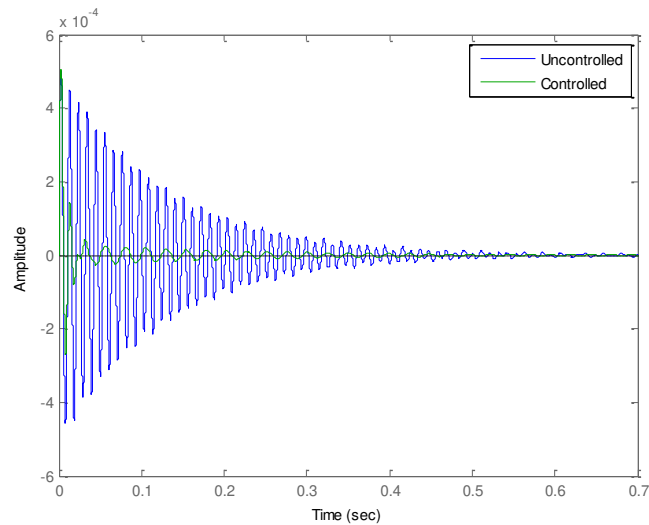
Figure 6-6 Vertical Spindle Impulse Response for Actuator Location 1

From the root locus plot, it was seen that some of the lower frequency poles had increased damping due to the controller. These lower frequency modes have little vertical spindle displacement but contain significant horizontal spindle displacement. The affect of this controller on these modes was also investigated. Figure 6-7 shows the x-axis frequency response of the spindle. The two lowest from this plot create the largest horizontal displacements. While not as large as the targeted frequency, there is still significant decibel reduction for these modes. Figure 6-8 shows the horizontal impulse response of the spindle. The two lower modes are dampened out fairly quickly while the higher frequency remains unaffected but with little amplitude.

Figure 6-7 Horizontal Spindle Frequency Response for Actuator Location 1
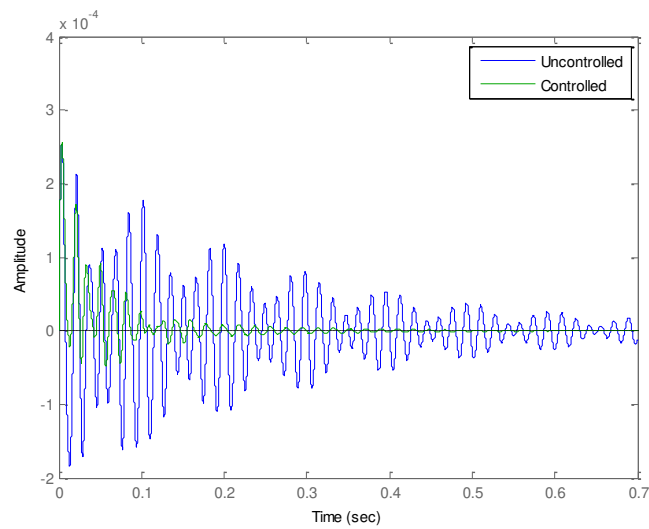
Figure 6-8 Horizontal Spindle Impulse Response for Actuator Location 1

Next the controller was tested for location 3 described in the previous chapter. The sensor/actuator pairs are placed on the outer beams just below the spindle arm brackets. As before, this controller is tuned for the frequency at 94 Hz. For this location the controller frequency was set at 103 Hz to maintain -90 degree phase shift for the targeted frequency. This is likely due to the influence of the next mode at 101 Hz. The controller damping remained at 0.4.

Figure 6-9 shows the root locus for tuning the controller gain for this controller. The poles are plotted for the controller gain varied from 0 to 130. For this actuator location, less control effort is required to draw the targeted poles into areas of higher damping. This also shows larger movements from the lower frequency structural poles. This is due to location 3 having more influence over these modes which was also shown in the dynamic responses of the previous chapter. There is room for increase in gain, as the controller poles are far from unstable. However, the structural poles see little benefit from increasing the gain. Also, the frequency response shows that the static stiffness is significantly reduced with higher gains for this actuator location.
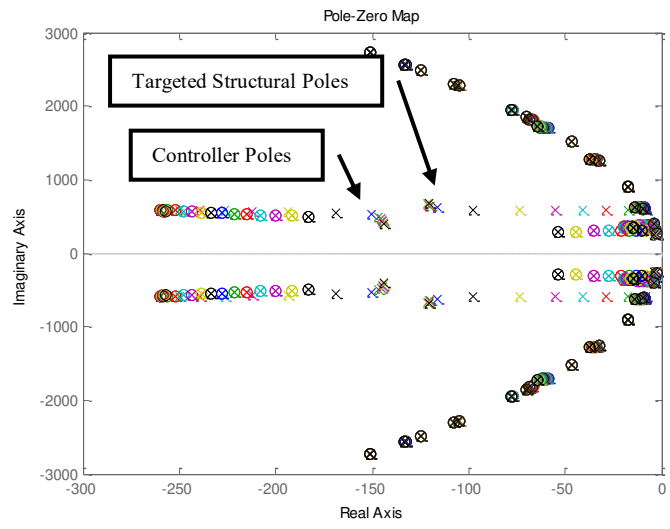
Figure 6-9 Root Locus Plot for Actuator Location 3

The vertical spindle frequency response is displayed in Figure 6-10. Similar decibel reduction is created for this controller as from the controller form location 1. This is, however, realized with a much lower gain than the controller from location 1. Care must be taken when tuning this controller as the static stiffness is easily decreased.
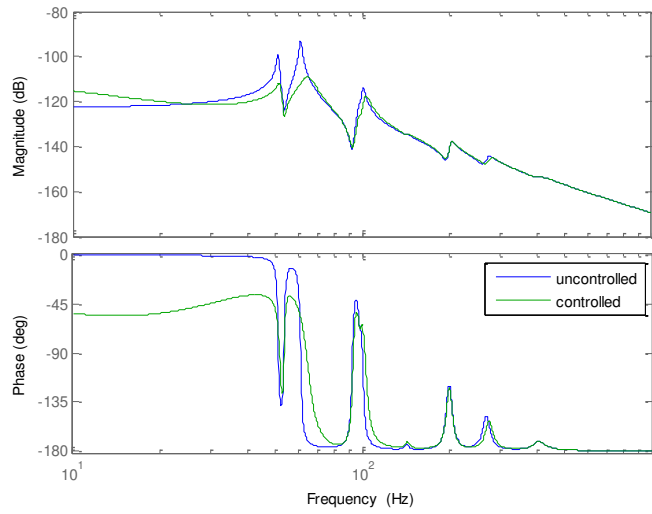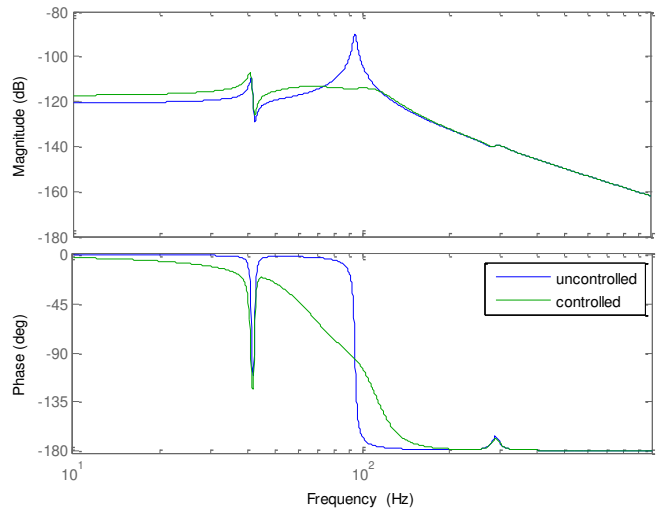
Figure 6-10 Vertical Spindle Frequency Response for Actuator Location 3
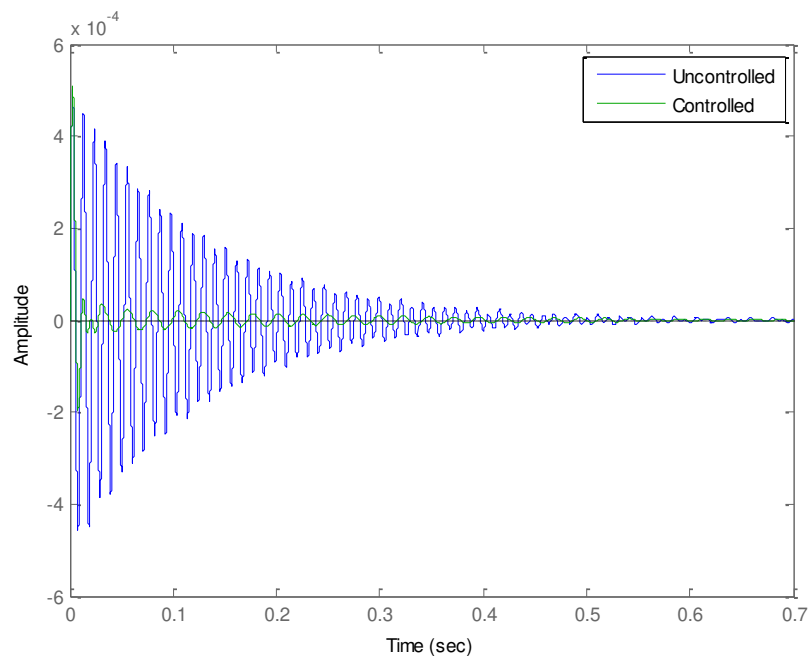
Figure 6-11 Vertical Spindle Impulse Response for Actuator Location 3

Figures 6-12 and 6-13 show the horizontal responses of the spindle with the actuator at location 3. Location 3 displays better ability to add damping to the two lower horizontal displacement modes than location 1. This can also be seen from the root locus plot as the lower frequency structural poles are easily drawn to locations of higher damping.
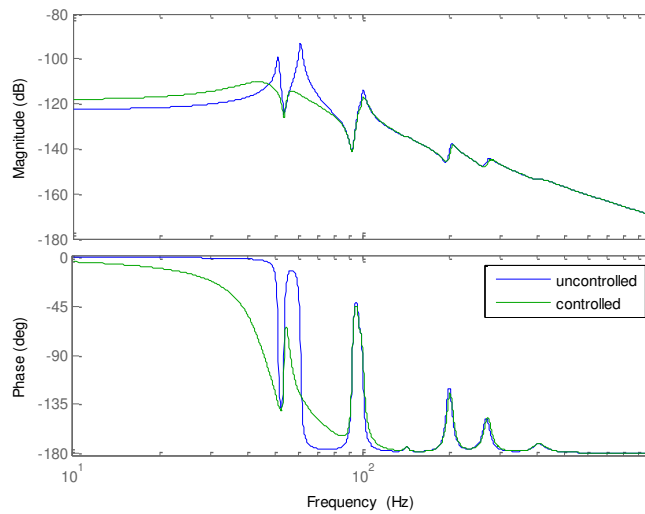
Figure 6-12 Horizontal Spindle Frequency Response for Actuator Location 3
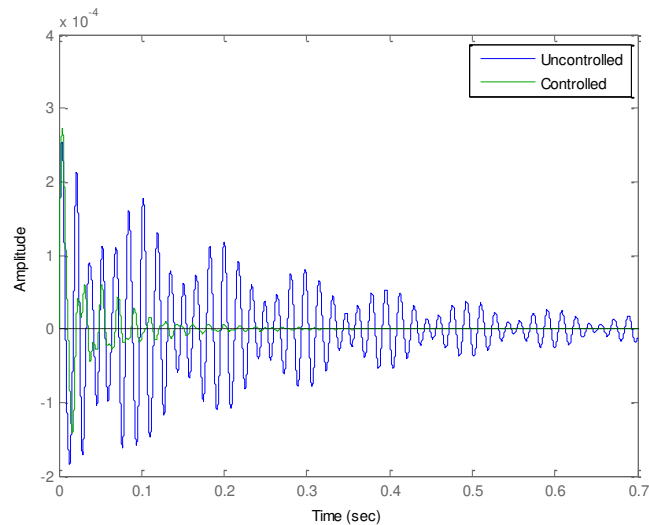
Figure 6-13 Horizontal Spindle Impulse Response for Actuator Location 3

Additional PPF controllers may be added to increase damping of modes not targeted by the first controller. This was done to target the two lower modes shown in the horizontal responses using actuators at location 3. When including multiple PPF controllers for one actuator, the filters are put in parallel. Therefore, the control signal is the summation of the outputs of the multiple PPF filters.

When tuning multiple PPF filters, the controllers are tuned from highest frequency down. This is done because a PPF filter may shift the frequencies of the lower modes as is seen from the previously tuned controller. The previously tuned controller maintained the same frequency and damping constants but required a lower controller gain. The gain for the controller targeting 94 Hz was reduced from 130 to 90. The new PPF controller used a controller frequency of 50 Hz, a damping ratio of 0.4, and a controller gain of 63. The resulting horizontal responses are

shown in Figures 6-14 and 6-15. This shows that the two lower horizontal critical modes can be

nearly removed completely. This is, however, at further expense of the static stiffness.
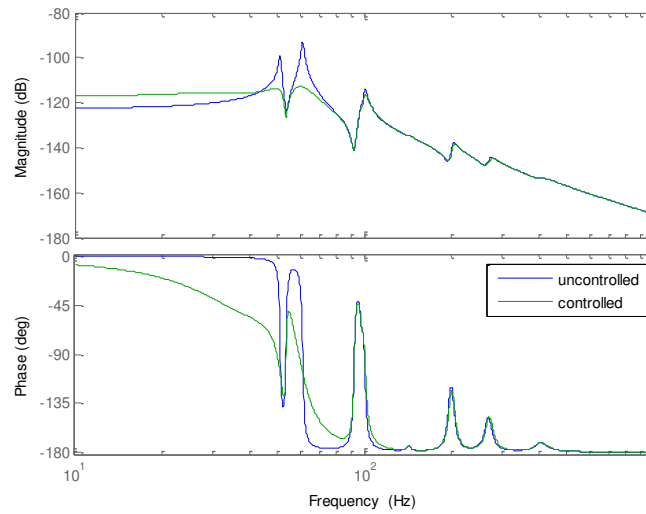
Figure 6-14 Horizontal Frequency Response of Spindle with Additional PPF
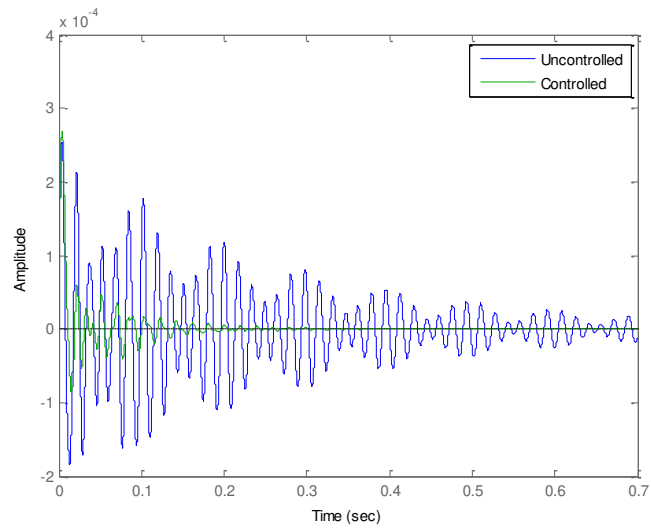
Figure 6-15 Horizontal Impulse Response of Spindle with Additional PPF

7   CHAPTER 7 - CONCLUSION AND RECOMENDATIONS

Finite Element Models of the Tetraform were created in both ANSYS and Matlab. The ANSYS model was used to conduct the modal analysis on the Tetraform. The resulting mode shapes were used to help determine which modes create displacements at the spindle location. They are also used to study which areas of the Tetraform contain the most vibrational energy for these modes. Both of FEA models can be used to study structural changes made to the Tetraform. The mode shapes from ANSYS are helpful in showing the changes in the displaced structure.

The Matlab model was converted to state space in order to plot frequency responses between different points on the structure. This shows the modal displacements relative to each other. These are insightful to how easily the modes are triggered by machining forces and external disturbances. This was also used to test the controllability of different actuator locations on the modes of interest. Finally, this state space model was used for active vibration control simulations

Positive Position Feedback Controllers were chosen as the active vibration control method and were designed to target the critical modes. The controllers were designed for actuators placed at locations 1 and 3. Both could significantly reduce the decibels of the target mode with the dominant vertical displacement of the spindle. Location 3 realized this decibel reduction with a much lower control effort. However, this location was much more prone to reducing the static stiffness of the Tetraform. Care must be taken when tuning PPF controller for

the Tetraform as reducing the static stiffness can be detrimental to the machining process. It was found that location 3 was more effective at targeting the lower frequency modes which create horizontal displacements to the spindle. Additional PPF controllers can be added to remove these lower modes, but once again, at the expense of static stiffness. This was a very effective way of adding damping to most critical modes. Therefore, this is very beneficial to the micro-machining process.

Some structural changes may also benefit the full scale Tetraform. One such change can stiffen the mode that contains significant vertical displacement of the spindle. The spindle holder and arms may be raised to a higher to a higher location on the Tetraform. This will shorten the spindle holder arms, stiffening this area of the mode shape. This will also transfer more energy to the lower portion of the Tetraform. The bottom brackets may also be removed to create more room for the linear position stages. This increases the transfer of more of the energy from some modes to the lower region. This also reduces the moving mass in this area for some modes, raising the frequency for these modes. It should be noted that these changes create a stronger resemblance between the full scale and 2/3 scale Tetraforms.

It is recommended that some adjustments be made to the tuning method of the PPF controllers. First, it should be converted over to optimal control. The controller should be tuned optimally based on target mode decibel reduction, maximizing static stiffness, and minimizing control effort. Also, the controller should be made adaptable. The structural poles change significantly with different structural modifications and different spindles. A method of online determination of the structural poles would be strongly recommended. It is also recommended to

include disturbance rejection control to supplement the vibration control to further stabilize the machining process.

APPENDIX A: MATLAB CODE

```
%Matlab Model Code for Frequency Response

%Define Material Properties
E=207e9;
p=7750;
G=79.3e9;
alpha=2;
beta=3e-5;



%Define Element Lengths
l1=.05754;
l2=.031115;
l3=.0254;
l4=.017356;
l5=.1234;
l6=.08467;
l7=.09017;
l8=.05855;
l9=.07366;
l10=.0254;
l11=.046533;


%Define Point Mass Inertias
m=2.6;  %sphere mass
ms=1.32+1.43;  %spindle holder mass
II=.002153;  %sphere mass moment
IIx=.001485+.00483;  %spindle holder mass moments
IIy=.001485+.00483;
IIz=.002225+.00036;


%Define Beam Cross Section Constants
%leg constants
A1=1.583e-4;   %leg area
Iy1=5.1877E-9;  %bending moments
Iz1=Iy1;
J1=2*Iy1;  %torsional constant

%leg w/ bracket1 constants
A2=.001717;
Iy2=2.1913e-7;
Iz2=3.6242e-7;
J2=Iy2+Iz2;

%leg w/ bracket2 constants
A3=.001799;
Iy3=2.5015e-7;
Iz3=3.7875e-7;
J3=Iy3+Iz3;

%leg w/ bracket3 constants
A4=.001813;
```

```matlab
Iy4=2.3331e-7;
Iz4=4.1742e-7;
J4=Iy4+Iz4;



%Cross Section Constants
y1=[Iy1;Iz1;J1;A1]; %leg
y2=[Iy2;Iz2;J2;A2]; %leg w/ bracket1
y3=[Iy3;Iz3;J3;A3]; %leg w/ bracket2
y4=[Iy4;Iz4;J4;A4]; %leg w/ bracket3

%Define Element Angles
%x=[xX;xY;xZ;yX;yY;yZ;zX;zY;zZ]
x1=[60;73;35;120;30;90;135;114;55].*(pi/180);
x2=[60;107;145;60;30;90;45;114;55].*(pi/180);
x3=[90;55;145;180;90;90;90;35;55].*(pi/180);
x4=[0;90;90;90;0;90;90;90;0].*(pi/180);
x5=[60;30;90;150;60;90;90;90;0].*(pi/180);
x6=[60;150;90;30;60;90;90;90;0].*(pi/180);
x7=[30;60;90;120;30;90;90;90;0].*(pi/180);
x8=[150;60;90;120;150;90;90;90;0].*(pi/180);
x9=[90;180;90;0;90;90;90;90;0].*(pi/180);
x10=[60;150;90;30;60;90;90;90;0].*(pi/180);
x11=[0;90;90;90;0;90;90;90;0].*(pi/180);
x12=[60;30;90;150;60;90;90;90;0].*(pi/180);
x=[x1,x2,x3,x4,x5,x6,x7,x8,x9];



%Empty Stiffness and Mass Matrices
K=zeros(101*6,101*6);
M=zeros(101*6,101*6);



%Element Properties (Each column is a different element)
    %Row1 --> element node 1
    %Row2 --> element node 2
    %Row3 --> element length
    %Row4-9 --> element angles
    %Row10-12--> element cross section constants


El=[1   4   5   6   7   8   9   10 11 12 13 14 15 16 17 18 19 20 21 22 23 24 25 26 27 28 29 30 17 31 32
33 34 35 36 37 38 39 40 41 42 43   1 44 45 46 47 48 49 50 51 52 53   1 54 55 56 57 58 59 60 61 62
63   3 64 65 66 67 68 69 70 71 72 73  56  74  75  61  76  77  51  78  79   9  80  81  82  83  84
85  86  25  87  88  89  90  91  92  93  38  94  95  96  97  98  99 100;
    4   5   6   7   8   9  10 11 12 13 14 15 16 17 18 19 20 21 22 23 24 25 26 27 28 29 30   2 31 32 33
34 35 36 37 38 39 40 41 42 43   3 44 45 46 47 48 49 50 51 52 53   2 54 55 56 57 58 59 60 61 62 63
3 64 65 66 67 68 69 70 71 72 73   2  74  75  46  76  77  66  78  79  71  80  81  82  83  84  85
86 101  87  88  89  90  91  92  93 101  94  95  96  97  98  99 100 101;
   11 11 11 11 11 12 12 13 14 14 14 15 15 15 15 15 15 15 14 14 14 13 12 12 11 11 11 11 15 15 15
15 14 14 14 13 12 12 11 11 11 11 16 16 16 17 18 18 18 17 16 16 16 16 16 16 17 18 18 18 17 16 16
16 16 16 16 17 18 18 18 17 16 16 16  17  19  17  17  19  17  17  19  17 110 110 111 111 111 111
111 111 110 110 111 111 111 111 111 111 110 110 111 111 111 111 111 111;
    x1 x1 x1 x1 x1 x1 x1 x1 x1 x1 x1 x1 x1 x1 x2 x2 x2 x2 x2 x2 x2 x2 x2 x2 x2 x2 x2 x2 x3 x3 x3
x3 x3 x3 x3 x3 x3 x3 x3 x3 x3 x3 x3 x4 x4 x4 x4 x4 x4 x4 x4 x4 x4 x4 x4 x5 x5 x5 x5 x5 x5 x5 x5 x5 x5
```

```
x5 x6 x6 x6 x6 x6 x6 x6 x6 x6 x6 x10 x10 x10 x11 x11 x11 x12 x12 x12  x7  x7  x7  x7  x7  x7
x7  x7  x8  x8  x8  x8  x8  x8  x8  x9  x9  x9  x9  x9  x9  x9  x9;
    y1 y1 y1 y1 y2 y2 y1 y1 y1 y1 y1 y1 y1 y1 y1 y1 y1 y1 y1 y1 y1 y1 y2 y2 y1 y1 y1 y1 y1 y1 y1
y1 y1 y1 y1 y1 y2 y2 y1 y1 y1 y1 y1 y1 y1 y4 y1 y1 y1 y4 y1 y1 y1 y1 y1 y1 y4 y1 y1 y1 y4 y1 y1
y1 y1 y1 y1 y4 y1 y1 y1 y4 y1 y1 y1  y4  y1  y4  y4  y1  y4  y4  y1  y4  y3  y3  y1  y1  y1  y1
y1  y1  y3  y3  y1  y1  y1  y1  y1  y1  y3  y3  y1  y1  y1  y1  y1  y1];


Ts=[]; %Sensor/Output Transformation Matrix

%Global Matrix Development
%Run a loop to fill the global matrix one element at a time
for i=1:length(El(1,:));

%Define Element Constants
Iy=El(13,i);
Iz=El(14,i);
J=El(15,i);
A=El(16,i);
L=El(3,i);


Te=[cos(El(4,i)) cos(El(5,i)) cos(El(6,i));
    cos(El(7,i)) cos(El(8,i)) cos(El(9,i));
    cos(El(10,i)) cos(El(11,i)) cos(El(12,i))];


%Element Coordinate Transformation Matrix
T=zeros(12,12);
T(1:3,1:3)=Te;
T(4:6,4:6)=Te;
T(7:9,7:9)=Te;
T(10:12,10:12)=Te;

%Sensor/Output Transformation Matrix
TS(i*12-11:i*12,i*12-11:i*12)=T;


% Both Timshenko and Classical Beam Elements were created and gave very
similar results.  Due to size of the Timoshenko matrices, only Classical
Elements are listed below.

%Define Beam Element Stiffness Matrix
Kel=[(A*E/L) 0 0 0 0 0 -(A*E/L) 0 0 0 0 0;
    0 (12*E*Iz/L^3) 0 0 0 (6*E*Iz/L^2) 0 -(12*E*Iz/L^3) 0 0 0 (6*E*Iz/L^2);
    0 0 (12*E*Iy/L^3) 0 -(6*E*Iy/L^2) 0 0 0 -(12*E*Iy/L^3) 0 -(6*E*Iy/L^2) 0;
    0 0 0 (G*J/L) 0 0 0 0 0 -(G*J/L) 0 0;
    0 0 -(6*E*Iy/L^2) 0 (4*E*Iy/L) 0 0 0 (6*E*Iy/L^2) 0 (2*E*Iy/L) 0;
    0 (6*E*Iz/L^2) 0 0 0 (4*E*Iz/L) 0 -(6*E*Iz/L^2) 0 0 0 (2*E*Iz/L) ;
    -(A*E/L) 0 0 0 0 0 (A*E/L) 0 0 0 0 0;
    0 -(12*E*Iz/L^3) 0 0 0 -(6*E*Iz/L^2) 0 (12*E*Iz/L^3) 0 0 0 -(6*E*Iz/L^2);
    0 0 -(12*E*Iy/L^3) 0 (6*E*Iy/L^2) 0 0 0 (12*E*Iy/L^3) 0 (6*E*Iy/L^2) 0;
    0 0 0 -(G*J/L) 0 0 0 0 0 (G*J/L) 0 0;
    0 0 -(6*E*Iy/L^2) 0 (2*E*Iy/L) 0 0 0 (6*E*Iy/L^2) 0 (4*E*Iy/L) 0;
    0 (6*E*Iz/L^2) 0 0 0 (2*E*Iz/L) 0 -(6*E*Iz/L^2) 0 0 0 (4*E*Iz/L)];
```

```matlab
%Define Beam Element Mass Matrix
Mel=[(140*p*A*L/420) 0 0 0 0 0 (70*p*A*L/420) 0 0 0 0 0;
    0 (156*p*A*L/420) 0 0 0 (22*p*A*L^2/420) 0 (54*p*A*L/420) 0 0 0 -
(13*p*A*L^2/420);
    0 0 (156*p*A*L/420) 0 -(22*p*A*L^2/420) 0 0 0 (54*p*A*L/420) 0
(13*p*A*L^2/420) 0;
    0 0 0 (p*J*L/3) 0 0 0 0 0 (p*J*L/6) 0 0;
    0 0 -(22*p*A*L^2/420) 0 (4*p*A*L^3/420) 0 0 0 -(13*p*A*L^2/420) 0 -
(3*p*A*L^3/420) 0;
    0 (22*p*A*L^2/420) 0 0 0 (4*p*A*L^3/420) 0 (13*p*A*L^2/420) 0 0 0 -
(3*p*A*L^3/420);
    (70*p*A*L/420) 0 0 0 0 0 (140*p*A*L/420) 0 0 0 0 0;
    0 (54*p*A*L/420) 0 0 0 (13*p*A*L^2/420) 0 (156*p*A*L/420) 0 0 0 -
(22*p*A*L^2/420);
    0 0 (54*p*A*L/420) 0 -(13*p*A*L^2/420) 0 0 0 (156*p*A*L/420) 0
(22*p*A*L^2/420) 0;
    0 0 0 (p*J*L/6) 0 0 0 0 0 (p*J*L/3) 0 0;
    0 0 (13*p*A*L^2/420) 0 -(3*p*A*L^3/420) 0 0 0 (22*p*A*L^2/420) 0
(4*p*A*L^3/420) 0;
    0 -(13*p*A*L^2/420) 0 0 0 -(3*p*A*L^3/420) 0 -(22*p*A*L^2/420) 0 0 0
(4*p*A*L^3/420)];




%Transform Element Stiffness Matrix
%Converts local element coordinates to global coordinates
%Transform Element Stiffness Matrix
Ke=T'*Kel*T;
%Transform Element Mass Matrix
Me=T'*Mel*T;




%Global Stiffness Matrix
%Puts the element stiffness matrix in the global matrix
K(El(1,i)*6-5:El(1,i)*6,El(1,i)*6-5:El(1,i)*6)=K(El(1,i)*6-
5:El(1,i)*6,El(1,i)*6-5:El(1,i)*6)+Ke(1:6,1:6);
K(El(1,i)*6-5:El(1,i)*6,El(2,i)*6-5:El(2,i)*6)=K(El(1,i)*6-
5:El(1,i)*6,El(2,i)*6-5:El(2,i)*6)+Ke(1:6,7:12);
K(El(2,i)*6-5:El(2,i)*6,El(1,i)*6-5:El(1,i)*6)=K(El(2,i)*6-
5:El(2,i)*6,El(1,i)*6-5:El(1,i)*6)+Ke(7:12,1:6);
K(El(2,i)*6-5:El(2,i)*6,El(2,i)*6-5:El(2,i)*6)=K(El(2,i)*6-
5:El(2,i)*6,El(2,i)*6-5:El(2,i)*6)+Ke(7:12,7:12);




%Global Mass Matrix
M(El(1,i)*6-5:El(1,i)*6,El(1,i)*6-5:El(1,i)*6)=M(El(1,i)*6-
5:El(1,i)*6,El(1,i)*6-5:El(1,i)*6)+Me(1:6,1:6);
M(El(1,i)*6-5:El(1,i)*6,El(2,i)*6-5:El(2,i)*6)=M(El(1,i)*6-
5:El(1,i)*6,El(2,i)*6-5:El(2,i)*6)+Me(1:6,7:12);
M(El(2,i)*6-5:El(2,i)*6,El(1,i)*6-5:El(1,i)*6)=M(El(2,i)*6-
5:El(2,i)*6,El(1,i)*6-5:El(1,i)*6)+Me(7:12,1:6);
```

```matlab
M(El(2,i)*6-5:El(2,i)*6,El(2,i)*6-5:El(2,i)*6)=M(El(2,i)*6-
5:El(2,i)*6,El(2,i)*6-5:El(2,i)*6)+Me(7:12,7:12);


end

%Sphere Mass Matrix
Msphere=[m 0 0 0 0 0;
         0 m 0 0 0 0;
         0 0 m 0 0 0;
         0 0 0 II 0 0;
         0 0 0 0 II 0;
         0 0 0 0 0 II];
%Spindle Holder Mass Matrix
Mspindle=[ms 0 0 0 0 0;
          0 ms 0 0 0 0;
          0 0 ms 0 0 0;
          0 0 0 IIx 0 0;
          0 0 0 0 IIy 0;
          0 0 0 0 0 IIz];


%Global Mass Matrix with Point Masses
M(1:6,1:6)=M(1:6,1:6)+Msphere;
M(2*6-5:2*6,2*6-5:2*6)=M(2*6-5:2*6,2*6-5:2*6)+Msphere;
M(3*6-5:3*6,3*6-5:3*6)=M(3*6-5:3*6,3*6-5:3*6)+Msphere;
M(17*6-5:17*6,17*6-5:17*6)=M(17*6-5:17*6,17*6-5:17*6)+Msphere;
M(101*6-5:101*6,101*6-5:101*6)=M(101*6-5:101*6,101*6-5:101*6)+Mspindle;


%Boundary Conditions
%Sphere at node 1 constrained in x,y and z directions
lv1=length(K(1,:));
K=K(4:lv1,4:lv1);
M=M(4:lv1,4:lv1);
TS=TS(4:lv1,4:lv1);


%Sphere at node 2 constrained in x,y and z directions
lv=length(K(1,:));
K=[K(1:3,:);K(7:lv,:)];
K=[K(:,1:3),K(:,7:lv)];
M=[M(1:3,:);M(7:lv,:)];
M=[M(:,1:3),M(:,7:lv)];
TS=[TS(1:3,:);TS(7:lv,:)];
TS=[TS(:,1:3),TS(:,7:lv)];


%Sphere at node 3 constrained in x,y and z directions
lv=length(K(1,:));
K=[K(1:6,:);K(10:lv,:)];
K=[K(:,1:6),K(:,10:lv)];
M=[M(1:6,:);M(10:lv,:)];
M=[M(:,1:6),M(:,10:lv)];
TS=[TS(1:6,:);TS(10:lv,:)];
TS=[TS(:,1:6),TS(:,10:lv)];
```

```matlab
%Solve for the Modal Matrix and Eigenvalues
[V,D]=eig(K,M);



%Sort Eigenvectors and Eigenvalues
[lambda,k]=sort(diag(D));
V=V(:,k);
Factor=diag(V'*M*V);
Vnorm=V*inv(sqrt(diag(Factor)));   %Normalized Modal Matrix
Mdiagonal=Vnorm'*M*Vnorm;
omega=diag(sqrt(Vnorm'*K*Vnorm));
nf2=omega./(2*pi);
V=Vnorm(:,1:60);   %Define number of included modes

%Modal Coordinates Matrices using Modal Matrix
Km=V'*K*V;
Mm=V'*M*V;



%STATE SPACE

%Input Matrix
h=zeros(length(K(1,:)),1);

%impulse
h(101*6-3-9,1)=1;



%Sensor Matrix
s=zeros(1,length(K(1,:)));
s(1,101*6-3-9)=1;

%Input transformation
h=TS'*h;

%Define Damping Matrix
Cd=alpha*Mm+beta*Km;



%A Matrix
UL=zeros(length(Km(1,:)),length(Km(1,:)));
UR=eye(length(Km(1,:)),length(Km(1,:)));
LL=(-inv(Mm))*Km;
LR=(-inv(Mm))*Cd;
A=[UL,UR;LL,LR];



%B Matrix
BU=zeros(length(Km(1,:)),1);
BL=inv(Mm)*V'*h;
B=[BU;BL];
```

106

```matlab
%C Matrix
CR=zeros(1,length(Km(1,:)));
CL=s*TS*V;
C=[CL,CR];

D=0;

G=ss(A,B,C,D);

w={10*2*pi,1000*2*pi};
h=bodeplot(G,w);
% Change units to Hz and make phase plot invisible
setoptions(h,'FreqUnits','Hz');
```

LIST OF REFERENCES

[1] Lindsey, K. (1991). Tetraform Grinding. *SPIE., Commercial applications of precision manufacturing at the sub-micron level*, *1573*, 129.

[2] Stephenson, D. J. et al. (2002). Ultra Precision Grinding using the Tetraform Concept. *Abrasives Magazine*, 12-16.

[3] Jackson, M. J. & Hyde, L. J. & Robinson, G. M. & Ahmed, W. (2006). Dynamic Response of a Tetrahedral Nanomachining Machine Tool Structure. *International Journal of Nanomanufacturing, 1 (1),* 26-46.

[4] Hyde, L. J. (2003). *Vibration Analysis of a Tetrahedral Structure*, Tennessee Technological University Master Thesis.

[5] Ma, L. (2008). *Design and Development of a Micromachining Tool Structure,* Purdue University Master Thesis.

[6] Manjunath, T. C. Mathematical Modeling of SISO based Timoshenko Structures-A Case Study. *International Journal of Mathematics Sciences*, *1 (1)*.

[7] Narayanan, S. & Balamurugan, V. (2003). Finite Element Modeling of Piezolaminated Smart Structures for Active Vibration Control with Distributed Sensors and Actuators. *Journal of Sound and Vibration*, *262*, 529-562.

[8] Fanson, J. L. & Caughey, T. K. (1990), Positive position feedback-control for large space structures. *AIAA Journal*, *28*, *4*, 717-724.

[9] Moheimani, S. O. & Fleming, A. J. (2006) *Piezoelectric Transducers for Vibration Control and Dampin.,* Springer-Verlag London Ltd.

[10] Inman, D. J. (2006). *Vibration with Control*. John Wiley & Sons, Ltd.

[11] Baillargeon, B. P. & Vel, S. S. (2005). Active Vibration Suppression of Sandwich Beams using Piezoelectric Shear Actuators: Experiments and Numerical Simulations. *Journal of Intelligent Material Systems and Structures, 16,* 517-530.

[12] *IEEE Standard on Piezoelectricity.* (1987). ANSI-IEEE Std, 176-187.

[13] Corbett, J., et al, 1999, An Ultra Precision Machine Tool Demonstrating a Novel Vibration Resistant Structure Precision Engineering – Nanotechnology, Proceedings of the 1st International eu**spen** Conference, 1, 159-162, Shaker Verlag, Aachen.

[14] Slocum, S. & Wilson, S. A. & Corbett, J. & Whatmore, R. W. Ultra-Precision Grinding of PZT Ceramics—Surface Integrity Control and Tooling Design. *International Journal of Machine Tools & Manufacture, 49,* 998–1007.

[15] Goh, C. J. & Caughey, T. K. (1985). On the Stability Problem Caused by Finite Actuator Dynamics in the Collocated Control of Large Space Structures. *International Journal of Control, 41,* 787-802.

[16] Friswell, M. I. & Inman, D. J. (1999). The Relationship Between Positive Position Feedback and Output Feedback Controllers. *Smart Materials and Structures, 8,* 285-291.

[17] Poh, S. & Baz, A. (1990). Active Control of a Flexible Structure Using a Modal Positive Position Feedback Controller. *Journal of Intelligent Material Systems and Structures, 1,* 273-288.

[18] Rao, S. S. (2004). *Mechanical Vibrations*. Pearson Education, Ltd.

[19] SAS, Inc. (2007). *ANSYS Element Reference*, Release 11.0.

[20] Mide Technologies (October 2009). Mide Engineering Smart Technologies. *http://www.mide.com/*